



Title	Short-term glacier velocity changes at West Kunlun Shan, Northwest Tibet, detected by Synthetic Aperture Radar data
Author(s)	Yasuda, Takatoshi; Furuya, Masato
Citation	Remote Sensing of Environment, 128, 87-106 https://doi.org/10.1016/j.rse.2012.09.021
Issue Date	2013-01-21
Doc URL	http://hdl.handle.net/2115/51782
Type	article (author version)
File Information	RSE128_87-106.pdf



[Instructions for use](#)

Short-term Glacier Velocity Changes at West Kunlun Shan, Northwest Tibet, Detected by Synthetic Aperture Radar Data

Takatoshi Yasuda and Masato Furuya

Department of Natural History Sciences, Graduate School of Science, Hokkaido University, N10W8, Kita-ku, Sapporo 060-0810, JAPAN.

Abstract

Seasonal glacier velocity changes across the High Arctic, including the Greenland Ice Sheet, have been observed and have attracted significant attention over the past decade. However, it remains uncertain how much short-term variability exists in other polythermal glaciers, particularly those in High Asia. Here we report satellite radar image analyses that reveal diverse glacier surface velocities and their evolution in West Kunlun Shan (WKS), NW Tibet, where little is known about glacier dynamics. On the basis of radar images obtained from 2003 to 2011, we examined 36 glaciers, and classified them into two classes according to their multi-temporal velocity profiles: 25 as normal-flow type (surface velocity reaches maxima around the middle part, and gradually approaches zero toward downstream and upstream), and four as surging type (surface velocities are greater than 150 m/yr, and/or the terminus advance is recognized from the radar images). Seven other glaciers do not fit the former two classes, and reveal stagnant velocity profiles that are nearly zero in the lower part but are similar to those of the normal type in the upper part. Although these glaciers could be just stagnant tongues

indicative of receding normal type glaciers, given the temporal evolution at the Zhongfeng Glacier, the stagnant type possibly represents a quiescent phase of the surging type glaciers. While glacier surfaces are mostly clean with limited debris-cover, except near the termini, surge-type glaciers might be common in WKS. The observed short-term velocity changes provide us with evidence for efficient basal slip even at the high-elevation polythermal glaciers. This study demonstrates that frequent radar image acquisitions are helpful to understand short-term velocity changes at remote glaciers in detail.

Keywords: glacier velocity, West Kunlun Shan, surge, SAR, PALSAR

1. Introduction

Glacier surface velocity is a combination of the internal deformation of the ice and basal slip, the latter of which consists of the basal sliding over the bedrock and the deformation of the till overlying the bedrock [Cuffey and Patterson, 2010]. As the speed associated with internal deformation can possibly vary over long periods, short-term surface velocity variations can be attributed to the basal slip due to reduction in the effective overburden pressure associated with changes in the hydrologic system [Iken and Bind-schadler, 1986]; by short-term we characterize velocity changes with timescale of less than a year. Such rapid signals detected over the past decade across the High Arctic, including the Greenland Ice Sheet, have been attracting considerable attention [e.g., Zwally et al., 2002; Rignot and Kanagaratnam, 2006; Joughin et al., 2008; Bartholomaus et al., 2008; Sundal et al., 2011], not only because they were believed to be absent from cold glaciers, but also because

15 surface melting in response to global warming could further accelerate glacier
16 flow and potentially lead to significant loss of glacier mass [e.g., Zwally et
17 al., 2002].

18 Due to the difficulty in directly monitoring glaciers in remote areas by
19 fieldwork, satellite remote sensing techniques such as radar interferometry
20 and pixel-offset tracking (or, feature/speckle tracking) of both optical and
21 radar imaging have been used to detect glacier velocities [e.g., Joughin et
22 al., 1996; Strozzi et al., 2002; Rignot and Kanagaratnam, 2006; Joughin et
23 al., 2008; Sundal et al., 2011; Gourmelen et al., 2011]. Besides the glaciers in
24 the High Arctic, these techniques have been applied to mountain glaciers in
25 High Asia and elsewhere [e.g., Kääb, 2005; Luckman et al., 2007; Quincey et
26 al., 2009, 2011; Scherler et al., 2011a, b; Mayer et al., 2011]. However, since
27 the previous studies focused on secular to interannual changes, the temporal
28 resolution was approximately a year. Thus, it remains unclear how much
29 short-term variability exists in the glaciers in High Asia.

30 Although our initial aim was to study the Yutian earthquake (magnitude
31 7.1) on March 20 2008 in West Kunlun Shan (WKS, Figure 1) [Furuya and
32 Yasuda, 2011], we accidentally detected significant glacier motion signals
33 over a wide area in addition to the coseismic deformation signals. Because
34 little is known about glacier dynamics in WKS, we began examining if the
35 glaciers were moving irrespective of the earthquake. Using multitemporal
36 surface velocity data from satellite-based radar imaging analysis, we found
37 that the glaciers were actively moving irrespective of earthquakes, and that
38 the glacier velocities unexpectedly exhibited a variety of spatial-temporal
39 changes. The purpose of this paper is to report our observations of the

40 surface velocity data in WKS with particular emphasis on the short-term
41 variabilities such as seasonal change and surge. Whereas the WKS glaciers
42 were considered cold-based glaciers, our observations indicate a variety of
43 spatial and temporal surface velocity changes, including seasonality, surging,
44 and quiescence. Moreover, we discuss the possible mechanisms for the short-
45 term variabilities.

46 **2. Study Area**

47 WKS is one of the highest regions in the world, and the main ridge varies
48 between 6000 and 6500 m above sea level. Compared to the Hindu Kush,
49 Karakoram, and Himalaya, the mean elevation of the glaciers in WKS is
50 concentrated near 6000 m, and the topographic relief is rather low [Scherler
51 et al., 2011b]. Although it is a difficult area to access, following a reconnais-
52 sance in 1985, the China–Japan Joint Glaciological Expedition to WKS was
53 executed in 1987 [Zheng et al., 1988]. The mean annual temperature and
54 precipitation near the snow line (5900 m) on the northern slopes of these
55 mountains were estimated to be -14.7°C and ~ 460 mm, respectively [Zhang
56 and Jiao, 1987]. Also, similar to the Himalaya [Ageta and Higuchi, 1984],
57 most of the precipitation occurs in summer from June to August [Zhang and
58 Jiao, 1987].

59 There are 278 glaciers along the main ridge of WKS with a total area
60 of 2711.57 km² [Shangguan et al., 2007], and they are assumed to be cold-
61 based to polythermal (subpolar) glaciers. Scherler et al. [2011a] regarded
62 the glaciers in WKS as the most continental setting in High Asia. Satellite-
63 based remote sensing has been performed to examine temporal changes in

64 the glaciated areas [Shangguan et al., 2007]; the total area loss observed
65 between 1970 and 2001 is at most 0.4%. On the basis of feature tracking
66 of the Advanced Spaceborne Thermal Emission and Reflection Radiometer
67 (ASTER) and Satellite Pour l’Observation de la Terre (SPOT) data, Scher-
68 ler et al. [2011b] showed the surface velocities of several glaciers in WKS.
69 However, these studies are based on optical imaging, and observation oppor-
70 tunities are limited due to cloud cover problems. Scherler et al. [2011a] also
71 showed that the glaciers in West Kunlun Shan have limited debris cover.

72 **3. Data and Analysis Method**

73 *3.1. Satellite data*

74 To generate glacier surface velocity maps, we processed the Phased Array-
75 type L-band (wavelength of 23.6 cm) Synthetic Aperture Radar (PALSAR)
76 images from the Advanced Land Observation Satellite (ALOS) launched in
77 2006 by the Japan Aerospace Exploration Agency (JAXA) from February
78 2007 to February 2011 (Table 1, Figure 1); see Shimada et al. [2008] for
79 details on the PALSAR. From 2003 to 2007, we also utilized the Advanced
80 Synthetic Aperture Radar (ASAR) images from the Environmental Satellite
81 (Envisat) launched in 2002 by the European Space Agency (Table 1, Figure
82 1). In comparison to an L-band sensor [Strozzi et al., 2008], the ASAR is a
83 C-band (wavelength of 5.6 cm) sensor that often suffers from decorrelation
84 problems due to its shallower penetration depth into snow and ice [Rignot
85 et al., 2001]. Nevertheless, we could extend the analysis period further to
86 find how the surface velocity of a surging glacier evolved over time. The
87 differences in the penetration depths by the different wavelengths will not

88 affect the inferred velocities, because the most significant changes in the
89 vertical velocity profile of glacier-flow are expected near the bed instead of
90 near the surface [Cuffey and Patterson, 2010].

91 The PALSAR data cover the study area along two ascending paths 515
92 and 516 over the two tracks, frame 690 and 700 (Table 1, Figure 1). The
93 off-nadir beam angle is 34.3° , which forms $\sim 38^\circ$ incident angle at the flat
94 ground in the image center. There are two imaging modes Fine Beam Single
95 polarization (FBS, HH) and Fine Beam Dual polarization (FBD; HH and
96 HV), respectively. We only used the HH polarization data. The difference
97 between FBS and FBD is within the range (across track) resolution, which is
98 ~ 4.7 m for the FBS and ~ 9.4 m for the FBD mode. The FBD data are over-
99 sampled twice along the range axis. On the other hand, the ASAR data used
100 in this study were obtained along a descending path with a local incidence
101 beam angle of $\sim 23^\circ$. The smaller incidence angle lowers the sensitivity to the
102 east–west component of the displacement although it can raise that of the
103 vertical component. The spatial resolution of ASAR in the range direction
104 is almost the same as the FBD mode of PALSAR, which is half of the FBS
105 mode.

106 *3.2. Surface velocity observations*

107 In this study, pixel-offset tracking (feature tracking or speckle tracking)
108 algorithms are used to observe surface velocities, and these algorithms are
109 based on maximizing the cross-correlation of the radar image patches [Michel
110 et al., 1999; Strozzi et al., 2002, 2008; Kobayashi et al., 2009]. We use the
111 intensity tracking algorithm, because it is the only technique that can be ap-
112 plied in the study of fast-flowing glaciers with long data acquisition interval

113 [Strozzi et al., 2002]. The method is also applicable to optical images. We
114 employed a search patch of ~ 300 m (range) \times 600 m (azimuth) area on the
115 ground with a sampling interval of ~ 56 m \times 56 m on the ground. We set
116 a signal-to-noise ratio (SNR) threshold of 5.0, and patches below this level
117 were assigned to the missing data. Lower SNR data are presumably due to
118 the large spatial separation length (baseline) of the repeating orbits (Bperp
119 in Table 1) and/or temporal changes in the surface scattering characteristics;
120 Bperp denotes the perpendicular component of the baseline projected onto
121 the radar line of sight (LOS). Unfortunately, the Bperp for the PALSAR data
122 pairs in summer was relatively long. Moreover, given the higher precipita-
123 tion and temperature in summer, we can consider that snowfall and surface
124 melting lowers the cross-correlation between the temporally separated im-
125 age patches, and prevent us from deriving summer velocities particularly in
126 the accumulation zones. Nonetheless, we emphasize that the surface velocity
127 data detected along the glacier itself are robust when compared with the
128 lack of significant changes outside the glaciated areas; we did not mask the
129 non-glacier areas in the offset-tracking.

130 While performing pixel-offset tracking, we corrected the stereoscopic ef-
131 fect, which is shown as an artifact offset over rugged terrain [Michel et
132 al., 1999; Kobayashi et al., 2009]. Because of the separation between satellite
133 orbital paths, the effect of fore-shortening also differs in the offsets. Thus,
134 we reduced the artifact by applying an elevation-dependent correction by
135 employing the NASA’s Shuttle Radar Topography Mission (SRTM-4) DEM
136 data with a 3-arcsec resolution, in which the gaps in the original SRTM
137 data were filled [Jarvis et al., 2008]. Note that the correction is different

138 from the elimination of topographic phase in the differential interferometric
139 phase measurement, and that the correction is unnecessary in the absence
140 of significant topography. Although the SRTM data may include their own
141 errors and are nearly a decade old, we used them because there were no gaps
142 and apparent noises. Because there are no topography-correlated offsets, we
143 consider that the stereoscopic correction is adequately performed, and it is
144 unlikely that the errors in the SRTM DEM influenced our velocity data.

145 The pixel-offset tracking technique provides us with two displacement
146 maps during the analyzed period; the range offset along the radar LOS
147 and the azimuth offset along the satellite-track direction. U_e , U_n , and U_z
148 were defined as eastward, northward, and upward positive displacements,
149 respectively. The range offset is a projection of the 3D surface displace-
150 ments onto the slant radar LOS direction, i.e., $0.62U_e+0.11U_n-0.78U_z$ for
151 ALOS and $-0.38U_e+0.08U_n-0.92U_z$ for Envisat; the azimuth offset is a pro-
152 jection of the 3D surface displacements along the satellite-track direction,
153 i.e., $-0.17U_e+0.99U_n$ for ALOS and $-0.21U_e-0.98U_n$ for Envisat. Therefore,
154 the range offset is sensitive to both the east-west and vertical components,
155 whereas the azimuth offset is most sensitive to the north-south component
156 and shows no sensitivity to the vertical component. We derived the surface
157 velocity data, following the parallel flow assumption [Joughin et al., 1996],
158 although the assumption is not strictly met in reality. In this study, we
159 used both the range and the azimuth offset components, so that the prob-
160 lem became over-determined and could be robustly solved by least-square
161 methods. The local topographic gradient unit vector was estimated from
162 a fore-mentioned SRTM-4 data. Although the elevation changes possibly

163 occurred between the SRTM and the PALSAR/ASAR data acquisition are
164 potential error sources, those changes would be insignificant for the computa-
165 tion of a unit vector, because only the local flow orientation and slope angles
166 are necessary in the argument of trigonometric functions for the parallel flow
167 approximation, and the ice thickness itself does not come into play.

168 The uncertainties of the offset measurements have been estimated to be
169 $\sim 0.3\text{--}0.4$ m at the rugged terrain on the basis of two data images with
170 ALOS/PALSAR's 46-day intervals acquired at non-deforming areas [Kobayashi
171 et al., 2009]. Assuming linear temporal evolution, the error in the velocity
172 estimates can be inferred to be 2–4 m/yr. However, the errors in pixel-offset
173 tracking can also arise from other sources. The longer the temporal separa-
174 tion, the smaller the errors in the velocity estimate, but the worse is the
175 correlation between the image patches due to changes in the scattering prop-
176 erties of the objects. Thus, most of the data pairs shown in this study have
177 the shortest possible 46-day and 35-day temporal separation, which denote
178 the PALSAR and ASAR return periods, respectively.

179 *3.3. Detecting scattering intensity changes*

180 Besides the surface velocity data, radar images can directly estimate the
181 extent of changes in glacier terminus locations if they are greater than sev-
182 eral tens of meters. Furthermore, the RGB method is a simple and useful
183 approach that can locate significant changes in the surface scattering inten-
184 sities [Tobita et al., 2006]. Representing the older scattering intensity image
185 with cyan [(Red, Green, Blue)=(0 %, 100 %, 100 %), Figure 2a], the newer
186 intensity image with red [(Red, Green, Blue)=(100 %, 0 %, 0 %), Figure 2b]
187 and adding the two images after co-registration, we can observe red/cyan

188 areas where surface scattering intensities increase/decrease, and areas with
189 no intensity changes remain gray (Figure 2c). Because we intentionally in-
190 creased/decreased the intensity in the west/east part in Figure 2b, there
191 arises an west-east gradient in the resulting Figure 2e. These two approaches
192 are particularly useful to demonstrate glacier surge signals.

193 4. Observation Results

194 4.1. Systematic examination and classification into two classes

195 Figure 3 is a sample glacier surface velocity map in WKS overlaid on the
196 PALSAR-based scattering intensity image. While the name of each glacier
197 is based on the World Glacier Inventory and partly on Ma et al. [1989], each
198 of the unnamed glaciers is merely numbered from the west to the east with
199 a prefix, representing the side of the slope on which it exists, i.e., N for
200 the northern and S for the southern slope. The velocities in Figure 3 are
201 estimated from the pair of PALSAR images acquired on November 12 and
202 December 30, 2008 for the western area (path 516), and the other pair of
203 images acquired on December 12, 2008 and January 28, 2009 for the eastern
204 area (path 515); see Table 1. As illustrated using a logarithmic scale, the
205 surface velocities reveal a variety of magnitudes, ranging within two orders
206 of magnitude (Figure 3). Although the available data do not cover all the
207 glaciers uniformly in terms of both the spatial and temporal distributions, we
208 examined systematically how the surface velocities varied in the 36 glaciers
209 in Figure 3. Setting a centerline at each valley glacier from the terminus
210 toward the up-glacier, we estimated the surface velocity profiles by averaging
211 the data over a $500 \times 500 \text{ m}^2$ area and regarded the standard deviations as the

212 estimated errors. When the number of data samples was less than half of the
213 total pixel numbers at each averaging area, or when the standard deviations
214 were larger than 30 m/yr, we considered them as missing data.

215 Examining the spatial–temporal evolution of surface velocities in each
216 glacier, we classify the 36 glaciers at WKS into normal–flow type, and surging
217 type. We describe below each type of surface velocity data, and show a
218 few typical examples; other glaciers’ data, not shown here, are listed in the
219 supplementary material. Seven of the examined glaciers, however, reveal
220 stagnant profiles, and do not fit the two classes. Those stagnant velocity
221 data and our interpretations on them are described in the Discussion.

222 *4.2. Normal Flow*

223 By a normal-flow type, we mean glaciers that continuously flow down-
224 stream without a stagnant zone, but exclude those with extremely rapid
225 velocities greater than 150 m/yr, which are grouped into the surging type.
226 Although it is not a commonly used threshold, the 150 m/yr limit is cho-
227 sen not only because other glaciers with similar slopes revealed much slower
228 velocities, but also because the surging type glaciers exhibited terminus ad-
229 vance as well as significant intensity changes as shown below. Among the
230 36 examined glaciers, we classified 25 into the normal–flow category (Table
231 2). None of the 25 glaciers exhibited significant interannual surface velocity
232 changes and terminus advances. Nonetheless, the magnitude of the surface
233 velocities is highly variable, depending on each glacier. We begin by showing
234 a few examples of the faster normal–flow glaciers.

235 Figures 4a and 4b show the spatial–temporal evolution of the surface
236 velocities and estimated errors, respectively, at the Duofeng Glacier, around

237 which the adjacent ALOS satellite tracks overlap and allow further increase
238 in the observation frequency. The Duofeng Glacier is the largest glacier in the
239 WKS originating in the northern side of Liushi Shan (Kunlun Goddess, 7167
240 m above sea level), the highest peak in the WKS. The respective terminus and
241 snowline altitudes are 4590 m and 5960 m above the sea level, and the mean
242 depth estimated from the empirical relation between the glacier thickness
243 and glacier area is 268 m [WGMS and NSIDC, 1989]. Although the inferred
244 velocities in Figure 4a are largely consistent with those independently derived
245 from optical images (see Figure 10c in Scherler et al., 2011b), the summer
246 velocities are evidently faster than those during winter. Shown in Figure 4c
247 are the velocity profiles averaged from winter and summer pairs. In addition,
248 the elevation and local gradient profiles along the flow line are shown in Figure
249 4d. While the average winter velocities from October to February are $70 \pm$
250 7 m/yr, those in summer from May to September are 92 ± 10 m/yr. As
251 shown in Figure 4c, however, the error bars are larger in summer, and the
252 summer velocity data are missing in the upper part. A significant separation
253 is found between 5 and 8 km from the terminus, where the summer and
254 winter average speeds are 92 m/yr and 64 m/yr, respectively.

255 Figures 5 and 6 show the results at the N3 Glacier and the eastern branch
256 of the Kunlun Glacier, respectively; the mean depths of the N3 and Kunlun
257 Glaciers are 194 m and 249 m, respectively [WGMS and NSIDC, 1989]. Due
258 to the large error bars particularly in summer, the summer speedup cannot be
259 clearly recognized as observed at the Duofeng Glacier. We don't conclude,
260 however, that summer speedup is absent in these glaciers. In Figures 4,
261 5, and 6, we could not derive a quality summer-velocity data particularly

262 in the upper accumulation zone partly because of long B_{perp} and the sur-
263 face scattering characteristics, which have changed significantly. In contrast,
264 we confirmed that the radar scattering intensities in the lower part did not
265 change appreciably, thereby aiding in the derivation of quality velocity data
266 even in summer. This was probably because the rugged ice surfaces in the
267 lower part could maintain intensity correlations with time; the rugged ice
268 surfaces generate a higher radar-scattering intensity than the surfaces in the
269 upper part, and they are also recognizable in the optical images of Google
270 EarthTM.

271 The observed summer speedup signals are significant, because velocities
272 above the winter average can be assumed to be due to basal sliding. The
273 basal-slip enhancement in summer can reach a maxima of ~ 30 m/yr between
274 5 and 8 km from the terminus of the Duofeng Glacier. Because the time scale
275 of the internal deformation variability is much longer than those of summer
276 speedup events, the ~ 40 % surface-velocity increase is unlikely due to the
277 increase in deformation velocity.

278 Most of the normal-flow glaciers, however, reveal slower winter velocities
279 than those in Figures 4, 5, and 6, despite the similar elevation profiles and
280 mean depths. Shown in Figures 7 and 8 are the results for the Yulong Glacier
281 and the eastern branch of the Kunlun Glacier, respectively; the mean depth
282 of Yulong is 223 m [WGMS and NSIDC, 1989]. Moreover, although there
283 appears to be a summer speedup near the terminus region in the eastern
284 branch of the Kunlun Glacier (Figure 8a and 8c), summer-velocity data are
285 missing, and the seasonalities remain uncertain in Figures 7 and 8. The
286 missing data for the summer in the slower glaciers is due to not only the

287 temporal changes in surface scattering characteristics but also the absence of
288 rugged surfaces, as found in the faster glaciers in Figures 4, 5, and 6, thereby
289 preventing the preservation of intensity correlations in summer.

290 *4.3. Surging type*

291 Using Envisat/ASAR radar images to extend the analysis period and
292 further analyze temporal changes in the radar intensities as well as the ter-
293 minus locations, we identify four glaciers as the surging type. The most
294 compelling evidence for surging was derived from the westernmost tributary
295 of the Zhongfeng Glacier in the southern slope. Moreover, we consider that
296 three extremely rapid glaciers in Figure 3, the West Kunlun, N2, and N7
297 Glaciers, are undergoing surge. Although Scherler et al. [2011b] mentioned
298 that stagnant glacier fronts were "most likely" due to past surges, they did
299 not show velocity data during the surge in WKS. On the basis of temporal
300 evolution of the velocity profile at the Zhongfeng Glacier's westernmost tribu-
301 tary, it turns out that surging is followed by stagnant flow near the terminus.
302 This is the first observation report of a glacier surge in WKS, to the best
303 of our knowledge. Although the upper part of the surge-type glaciers cer-
304 tainly appears white, and it is difficult to tell any looped or folded moraines,
305 we could recognize medial moraines in the Zhongfeng, N2, and West Kun-
306 lun Glaciers from the optical images available on Google EarthTM. These
307 observations could also corroborate the surging nature of the glaciers.

308 Figures 9 show spatial-temporal changes in the surface velocities and re-
309 lated data for the westernmost tributary of the Zhongfeng Glacier. Although
310 it is uncertain when exactly the surge initiated and terminated, Figure 9a
311 illustrates that the surface velocities exceeded 1000 m/yr over the wide area

312 along the glacier at least for half a year from 2004 to 2005, followed by a slow
313 down in 2006. Since 2007, the surface-velocity data indicate the stagnant
314 flow, in which almost all the lower half of the entire glacier has virtually
315 stopped, whereas the upper half moves. We observed that after the peak of
316 the surging phase, the surface velocities gradually decreased from ~ 100 m/yr
317 in 2007 to ~ 30 m/yr in 2010. The temporal duration of the slowdown phase
318 spans ~ 3 years, which is much longer than that after the 1982-1983 surge at
319 the Variegated Glacier [Kamb et al., 1985]. The detected spatial-temporal
320 evolution in the surface-velocity data presumably indicates a dynamic evo-
321 lution in the basal environment.

322 Next, we show the significant scattering intensity changes that could be
323 interpreted as quiescent changes in the surface roughness. Representing the
324 images acquired on February 9, 2007 and February 20, 2011 with cyan and
325 red, respectively, we derive a composite image in Figure 10. Because the orig-
326 inal two images were obtained on similar seasons, we may neglect seasonal
327 effects such as snow-fall and surface melting. Figure 10 shows an apparent
328 decrease in the scattering intensity at the surging tributary, whereas the other
329 tributaries to the east remained nearly the same. The period in Figure 10 is
330 a quiescent phase, when the surface velocities became gradually slower (Fig-
331 ure 9a). Because the scattering intensity generally decreases as the scattering
332 surface becomes smoother, our interpretation of intensity reduction is that
333 the rugged surfaces generated by the preceding surge are gradually recover-
334 ing to their original smoother forms by, for instance, a closure of crevasses
335 and/or cracks. Although this interpretation needs to be verified by other in-
336 dependent observations, we elucidate another example that indicates drastic

337 increase in the scattering intensity, which can be associated with an ongoing
338 surge.

339 Figures 11 and 12 show the results for the West Kunlun and the N2
340 Glaciers, respectively; the result for the N7 Glacier is in the supplementary
341 materials. The velocities at these two glaciers were as high as 170–200 m/yr
342 from November 2008 to February 2009 (Figure 11a and 12a). Although
343 they are slower than the peak velocities at the Zhongfeng Glacier shown
344 in Figure 9, these are much faster than the adjacent western tributary of
345 the West Kunlun Glacier, whose maximum speed is ~ 20 m/yr despite the
346 similar elevation and slope profiles in all three glaciers. Also, as observed at
347 the surge-type glaciers in Karakoram [Quincey et al., 2011], the velocities
348 reach maximum values near the lowermost part at the two glaciers. At the
349 N2 Glacier (Figure 12), the peak surface velocities from late 2008 to 2009
350 were preceded by an acceleration phase at least from 2007 to 2008, which is
351 again similar to the findings of surge-type glaciers in Karakoram [Quincey et
352 al., 2011].

353 Moreover, we identified a rapid advance in the termini initiated around
354 late 2008 – early 2009 (Figure 13) by visually tracking the terminus locations
355 in the intensity images. None of the other non-surging glaciers exhibited
356 significant advances in the terminus location. We recorded the amount of
357 advance, and found that the N2 Glacier advanced by 105 m from August to
358 October 2009. Although the most rapid advance ceased in 2009, the surging
359 continued until the end of the study period. The exact timing of the initiation
360 and termination of the surge remains uncertain, but the temporal duration
361 seems to be at least longer than half a year at the N2 Glacier. Figure 11

362 also suggest years' long surge duration at the West Kunlun Glacier. To place
363 stricter constraints, however, we need to extend the analysis period further.

364 Figure 14 is a composite image derived via the RGB method, using the
365 images same as those in Figure 10; it reveals red-colored areas in the West
366 Kunlun and N2 Glaciers, indicating recent drastic increases in the scatter-
367 ing intensities. This is contrary to the case in Figure 10, probably indicat-
368 ing that the surface became more rugged due to the drastic increase in the
369 crevasses/cracks associated with surging.

370 5. Discussion

371 5.1. Stagnant flow

372 Seven glaciers were not classified into either normal or surging type (Table
373 2), because they reveal very small surface velocities near the lower part of
374 the glacier but active motion in the upper part. Figures 15, 16, and 17 show
375 the surface velocities and related data for the Chongce, West Yulong, and
376 the second branch of the Zhongfeng Glacier, respectively. Summer speedup
377 signals were not as significant as we could recognize in Figure 4. We could
378 not find any significant changes in both the terminus locations and scattering
379 intensities, either.

380 In analogy with the velocity evolution at the westernmost tributary of the
381 Zhongfeng Glacier (Figure 9), the stagnant glaciers may represent a quies-
382 cent phase of surge cycles. Also, the longitudinal velocity profiles are consis-
383 tent with the well-known thermal structure of polythermal surging glaciers
384 at Bakaninbreen and Monacobreen, Svalbard [Murray et al., 1998, 2000,
385 2003] and Trapridge Glacier, Yukon, Canada [Clarke et al., 1984; Frappé

386 and Clarke, 2007]. The downstream resistance due to thermal structure ap-
387 pears to be a common factor. Although the glaciers in WKS have not been
388 considered as the surge type, and terminus elevations are higher than those
389 observed in the central Karakoram [Hewitt, 2007], implying a much colder
390 climate, these observations indicate that glacier surges in WKS could be com-
391 mon and widely distributed, suggesting that nearly one third of the examined
392 36 glaciers could be of the surge type.

393 However, it is also possible that the observed velocity distributions may
394 simply represent stagnant tongues of receding normal glaciers, because if
395 the terminus region is actually very thin and gently sloping, slow terminal
396 zones are possible. Long-term velocity observations are necessary to answer if
397 each stagnant glacier is normal type or surging type. However, the observed
398 surface gradients in panel (d) of Figures 15–17 are not particularly low, when
399 compared with those for other studied glaciers. We thus consider that those
400 are likely to be surge-type glaciers in quiescence.

401 The basal temperature was recorded to be -2.1 °C at a depth of ~ 300 m
402 at the Guliya Icecap (over 6000 m above sea level, Figure 1), where ~ 300 m
403 ice-core data have been sampled in the early 1990s [Thompson et al., 1995].
404 To the best of our knowledge, no other basal temperature data are available
405 for the remaining glaciers in WKS, and, in fact, they could be near the
406 melting point. The thermal structure of these glaciers needs to be examined
407 to understand the glacier dynamics in WKS better.

408 *5.2. Possible Surging Mechanisms in WKS*

409 A dynamic evolution of the subglacial hydrological system has been sug-
410 gested to explain rapid velocity changes [e.g., Kavanaugh and Clarke, 2001;

411 Mair et al., 2003; Bartholomaus et al., 2008; Schoof, 2010] and glacier surge
412 [e.g., Clarke et al., 1984; Kamb, 1987]. Regarding the physics of surging, the
413 extent of influence of the deformation of subglacial till on the disruptions of
414 subglacial hydrological systems has also been discussed [Truffer et al., 2000;
415 Harrison and Post, 2003].

416 Although water storage is essential to control any surging event, it re-
417 mains unclear whether there is sufficient volume of meltwater supply, be-
418 cause sublimation is more important than melting for ablation mechanism
419 under the cold and arid environment of WKS [Ageta et al., 1989]. While
420 the overall retreat of glaciers in WKS shown by Scherler et al. [2011a] may
421 suggest increased surface melt due to long-term climate change, our obser-
422 vations indicate that not all the glaciers reveal short-term velocity changes.
423 Although Clarke et al. [1986] concluded that it was not a likely mechanism
424 for surging, a thermal triggering mechanism that does not require surface
425 meltwater has been proposed to result in the surge in polythermal glaciers
426 [e.g., Clarke, 1976]. The cold environment can help develop a relatively thick
427 ice that could thermally insulate its basal layer, which can start melting be-
428 cause of the overburden pressure and/or geothermal heat flux and will form a
429 subglacial hydrological system to control the initiation and termination of the
430 surge [Clarke et al., 1976; Fowler et al., 2001]. Clarke et al. [1984], however,
431 did not find evidence for trapped water increasing the pore pressure. In-
432 stead, they suggested a reduction in the discharging capacity associated with
433 the deformation of the permeable substrate. The WKS area is tectonically
434 active not only as exemplified by the 2008 Yutian earthquake [Furuya and
435 Yasuda, 2011] but also by the Kunlun volcano group located ~ 30 km to the

436 northeast, where the latest eruption was witnessed in 1951, and 70 volcanic
437 cones are well-preserved [Liu and Maimaiti, 1989; Siebert and Simkin, 2002].
438 These geological settings are consistent with the previous findings that surg-
439 ing glaciers occur in tectonically active mountain ranges, whose glacier beds
440 tend to be deformable sediment [Cuffey and Patterson, 2010]. As the basal
441 till emerges near the terminus in WKS [Zheng et al., 1989], till deformation
442 may also be related to the surging events [e.g., Truffer et al., 2000]. More-
443 over, although it is speculative, the elevated geothermal heat flux cannot be
444 ignored as a possible cause for meltwater generation.

445 We can recall that in WKS, the glaciers are almost debris free and with
446 clean ice [Zheng et al., 1989; Scherler et al., 2011a]. Although glacier surges
447 have often been reported in debris-rich glaciers [Harrison and Post, 2003;
448 Barrand and Murray, 2006], our observations of surges in WKS suggest that
449 the debris cover is not an indispensable attribute for surge-type glaciers, and
450 that surging events on clean glaciers may have gone unnoticed. Nonetheless,
451 although the upper part of the surging glaciers certainly appears white, we
452 can recognize the debris-rich ice near the terminus as well as medial and
453 terminal moraines in the Zhongfeng, N2, and West Kunlun Glaciers from
454 the optical images available on Google EarthTM, consistent with the field
455 observation report by Zheng et al. [1989]. It is likely that they were generated
456 from basal erosion during previous surges. Quincey et al. [2011] reported
457 two surge type glaciers with clean ice in Karakoram, and related the findings
458 to a possible recent tendency of the Karakoram surges to be controlled by
459 thermal rather than hydrological conditions. Whereas surges on clean-ice
460 glaciers were unknown in Karakoram, our observations in WKS suggest that

461 surges on mostly clean-ice glaciers could be common.

462 **6. Conclusions**

463 By applying the pixel-offset tracking (feature tracking) technique to SAR
464 images, we examined spatial and temporal variabilities in the surface velocity
465 of 36 glaciers in WKS. Although the WKS glaciers have been assumed to be
466 mostly cold-based because of the cold, arid environment at high elevation, we
467 found clear summer speedup signals in nine glaciers as well as surging signals
468 in four glaciers. These short-term surface velocity changes provide us with
469 the evidence for effective basal slip in WKS. Given the velocity evolution data
470 for the Zhongfeng Glacier, the stagnant glaciers may represent a quiescent
471 phase, although they could be simply normal glaciers with thinner and gently
472 sloping terminal zones.

473 **7. Acknowledgement**

474 PALSAR level 1.0 data in this study were provided by the PALSAR Inter-
475 ferometry Consortium to Study our Evolving Land surface (PIXEL) and the
476 ALOS 3rd PI project under cooperative research contracts with the JAXA.
477 The ownership of PALSAR data belongs to JAXA and the Ministry of Econ-
478 omy, Trade and Industry. Envisat data are copyrighted by ESA and were
479 provided under Cat-1 project 7344. We thank S. Sugiyama and R. S. An-
480 derson for reading an earlier draft, and also thank two anonymous reviewers
481 for their constructive comments. We acknowledge the ESPEC Foundation
482 for Global Environment Research and Technology for supporting this study.
483 This study is partially supported by KAKENHI (24651001).

484 **References**

485 Ageta, Y., & K. Higuchi. (1984). Estimation of mass balance components
486 of a summer-accumulation type glacier in the Nepal Himalaya, *Geogr. Ann.*
487 *Ser. A, Phys. Geogr.*, 66, 249–255, <http://dx.doi.org/10.2307/520698>.

488 Ageta, Y., W. Zhang, & M. Nakawo. (1989). Mass balance studies on
489 Chongce Ice Cap in the West Kunlun Mountains, *Bull. Glacier Res.*, 7,
490 37–43.

491 Bartholomaus, T. C., R. S. Anderson, & S. P. Anderson. (2008). Response
492 of glacier basal motion to transient water storage, *Nat. Geosci.*, 1, 33–37,
493 <http://dx.doi.org/10.1038/ngeo.2007.52>.

494 Barrand, N. E., & T. Murray. (2006). Multivariate controls on
495 the incidence of glacier surging in the Karakoram Himalaya, *Arct.*
496 *Antarct. Alp. Res.*, 38(4), 489–498, [http://dx.doi.org/10.1657/1523-](http://dx.doi.org/10.1657/1523-0430(2006)38[489:MCOTIO]2.0.CO;2)
497 [0430\(2006\)38\[489:MCOTIO\]2.0.CO;2](http://dx.doi.org/10.1657/1523-0430(2006)38[489:MCOTIO]2.0.CO;2).

498 Clarke, G. K. C. (1976). Thermal regulation of glacier surging, *J. Glaciol.*,
499 16, 231–250.

500 Clarke, G. K. C., S. G. Collins, & D. E. Thomson. (1984). Flow, thermal
501 structure, and subglacial conditions of a surge-type glacier, *Can. J. Earth*
502 *Sci.*, 21(2), 232–240.

503 Clarke, G. K. C., J. P. Schmok, C. M. L. Ommanney, & S. G. Collins.
504 (1986). Characteristics of Surge-Type Glaciers, *J. Geophys. Res.*, 91(B7),
505 7165–7180.

- 506 Cuffey, K. M., & W. S. B. Paterson. (2010). *The Physics of Glaciers*, 4th
507 ed., Elsevier.
- 508 Frappé, T.-P., & G. K. C. Clarke. (2007). Slow surge of Trapridge
509 Glacier, Yukon Territory, Canada, *J. Geophys. Res.*, 112, F03S32,
510 <http://dx.doi.org/10.1029/2006JF000607>.
- 511 Fowler, A. C., T. Murray, & F. S. L. Ng. (2001). Thermally controlled glacier
512 surging, *J. Glaciol.*, 47, 527-538.
- 513 Furuya, M., & T. Yasuda. (2011). The 2008 Yutian normal fault-
514 ing earthquake (Mw 7.1), NW Tibet: Non-planar fault modeling
515 and implications for the Karakax Fault, *Tectonophys.*, 511, 125–133,
516 <http://dx.doi.org/10.1016/j.tecto.2011.09.003>.
- 517 Gourmelen, N., S. W. Kim, A. Shepherd, J. W. Park, A. V. Sundal, H.
518 Björnsson, & F. Pálsson. (2011). Ice velocity determined using conven-
519 tional and multiple-aperture InSAR, *Earth Planet. Sci. Lett.*, 307, 156–160,
520 <http://dx.doi.org/10.1016/j.epsl.2011.04.026>.
- 521 Harrison, W. D., & A. S. Post. (2003). How much do we really know about
522 glacier surging?, *Ann. Glaciol.*, 36, 1–6.
- 523 Hewitt, K. (2007). Tributary glacier surges: an exceptional concentration
524 at Panmah Glacier, Karakoram Himalaya, *J. Glaciol.*, 53(181), 181–188.
- 525 Iken, A., & R. A. Bindschadler. (1986). Combined measurements of
526 subglacial water pressures and surface velocity of the Findelengletscher,
527 Switzerland. Conclusions about drainage systems and sliding mechanism,
528 *J. Glaciol.*, 32, 101–119.

529 Jarvis A., H. I. Reuter, A. Nelson, & E. Guevara. (2008). Hole-filled seam-
530 less SRTM data V4, International Centre for Tropical Agriculture (CIAT),
531 available from <http://srtm.csi.cgiar.org>.

532 Joughin, I., R. Kwok, & M. Fahnestock. (1996). Estimation of ice-sheet
533 motion using satellite radar interferometry: Method and error analysis with
534 application to Humboldt Glacier, Greenland, *J. Glaciol.*, 42, 564–575.

535 Joughin, I., S. B. Das, M. A. King, B. E. Smith, I. M. Howat, & T. Moon.
536 (2008). Seasonal speedup along the western flank of the Greenland ice sheet,
537 *Science*, 320, 781–783, <http://dx.doi.org/10.1126/science.1153288>.

538 Kavanaugh, J. L., & G. K. C. Clarke. (2001). Abrupt glacier motion and re-
539 organization of basal shear stress following the establishment of a connected
540 drainage system, *J. Glaciol.*, 47, 472–480.

541 Kääh, A. (2005). Combination of SRTM3 and repeat ASTER data for de-
542 riving alpine glacier flow velocities in the Bhutan Himalaya, *Remote Sens.*
543 *Environ.*, 94, 463–474, <http://dx.doi.org/10.1016/j.rse.2004.11.003>.

544 Kamb, B., C. F. Raymond, W. D. Harrison, H. Engelhardt, K. A.
545 Echelmeyer, N. Humphrey, M. M. Brugman, & T. Pfeffer. (1985). Glacier
546 surge mechanism: 1982–1983 surge of Variegated Glacier, Alaska, *Science*,
547 227, 469–479.

548 Kamb, B. (1987). Glacier surge mechanism based on linked cavity configu-
549 ration of the basal water conduit system, *J. Geophys. Res.*, 92, 9083–9100.

550 Kobayashi, T., T. Takada, M. Furuya, & M. Murakami. (2009). Lo-
551 cations and types of ruptures involved in the 2008 Sichuan earthquake

552 inferred from SAR image matching, *Geophys. Res. Lett.*, 36, L07302,
553 <http://dx.doi.org/10.1029/2008GL036907>.

554 Liu, J., & Y. Maimaiti. (1989). Distribution and ages of Ashikule volcanoes
555 on the West Kunlun Mountains, west China, *Bull. Glacier Res.*, 7, 187–190.

556 Luckman, A., D. J. Quincey, & S. Bevan. (2007). The potential of satel-
557 lite radar interferometry and feature tracking for monitoring flow rates of
558 Himalayan glaciers, *Remote Sens. Environ.*, 111(2–3), 172–181.

559 Ma, Q., B. Zheng, K. Jiao, S. Iwata, & H. Fushimi. (1989). Glacial geomor-
560 phological features in upper reaches of Yurunkax River on the north slope
561 of the West Kunlun Mountains, *Bull. Glacier Res.*, 7, 139–144.

562 Mair, D., I. Willis, U. H. Fischer, B. Hubbard, P. Nienow, & A. Hubbard.
563 (2003). Hydrological controls on patterns of surface, internal and basal mo-
564 tion during three ‘spring events’: Haut Glacier d’Arolla, Switzerland, *J.*
565 *Glaciol.*, 49, 555–567.

566 Mayer, C., A. C. Fowler, A. Lambrecht, & K. Scharrer. (2011). A surge of
567 North Gasherbrum Glacier, Karakoram, China. *J. Glaciol.*, 57(204), 904–
568 916.

569 Michel, R., J.-P. Avouac, & J. Taboury. (1999). Measuring ground displace-
570 ments from SAR amplitude images: Application to the Landers Earthquake,
571 *Geophys. Res. Lett.*, 26, 875–878.

572 Murray, T., J. A. Dowdeswell, D. J. Drewry, & I. Frearson. (1998). Geomet-
573 ric evolution and ice dynamics during a surge of Bakaninbreen, Svalbard, *J.*
574 *Glaciol.*, 44, 263–272.

575 Murray, T., G. W. Stuart, P. J. Miller, J. Woodward, A. M. Smith, P. R.
576 Porter, & H. Jiskoot. (2000). Glacier surge propagation by thermal evolution
577 at the bed, *J. Geophys. Res.*, 105(B6), 13491–13507.

578 Murray, T., T. Strozzi, A. Luckman, H. Jiskoot, & P. Christakos. (2003). Is
579 there a single surge mechanism? Contrasts in dynamics between glacier
580 surges in Svalbard and other regions, *J. Geophys. Res.*, 108(B5), 2237,
581 <http://dx.doi.org/10.1029/2002JB001906>.

582 Quincey, D. J., L. Copland, C. Mayer, M. Bishop, A. Luckman, & M. Beló.
583 (2009). Ice velocity and climate variations for Baltoro Glacier, Pakistan, *J.*
584 *Glaciol.*, 55, 1061–1071, <http://dx.doi.org/10.3189/002214309790794913>.

585 Quincey, D. J., M. Braun, N. F. Glasser, M. P. Bishop, K. Hewitt, & A.
586 Luckman. (2011). Karakoram glacier surge dynamics, *Geophys. Res. Lett.*,
587 38, L18504, <http://dx.doi.org/10.1029/2011GL049004>.

588 Rignot, E., K. Echelmeyer, & W. Krabill. (2001). Penetration depth of
589 interferometric synthetic aperture radar signals in snow and ice, *Geophys.*
590 *Res. Lett.*, 28(18), 3501–3504.

591 Rignot, E. and P. Kanagaratnam. (2006). Changes in the velocity struc-
592 ture of the Greenland ice sheet, *Science*, 311, 986–990, <http://dx.doi.org/10.1126/science.1121381>.

594 Scherler, D., B. Bookhagen, & M. R. Strecker. (2011a). Spatially variable
595 response of Himalayan glaciers to climate change affected by debris cover,
596 *Nat. Geosci.*, 4, 156–159, <http://dx.doi.org/10.1038/ngeo1068>.

- 597 Scherler, D., B. Bookhagen, & M. R. Strecker. (2011b). Hillslope-glacier
598 coupling: The interplay of topography and glacial dynamics in High Asia,
599 *J. Geophys. Res.*, 116, F02019, <http://dx.doi.org/10.1029/2010JF001751>.
- 600 Schoof, C. (2010). Ice-sheet acceleration driven by melt supply variability,
601 *Nature*, 468, 803–806, <http://dx.doi.org/10.1038/nature09618>.
- 602 Shangguan, D., S. Liu, Y. Ding, J. Li, Y. Zhang, L. Ding, X. Wang, C. Xie,
603 & G. Li. (2007). Glacier changes in the west Kunlun Shan from 1970 to 2001
604 derived from Landsat TM/ETM+ and Chinese glacier inventory data, *Ann.*
605 *Glaciol.*, 46, 204–208, <http://dx.doi.org/10.3189/172756407782871693>.
- 606 Shimada, M., Y. Fukushima, T. Ozawa, M. Furuya, & A. Rosenqvist.
607 (2008). Japanese L-band radar improves surface deformation monitoring,
608 *EOS, Trans. Am. Geophys. Union*, 89 (31), 277–278.
- 609 Siebert, L., & T. Simkin. (2002-). *Volcanoes of the World: an Illus-*
610 *trated Catalog of Holocene Volcanoes and their Eruptions*. Smithsonian
611 Institution, Global Volcanism Program Digital Information Series, GVP-3,
612 (<http://www.volcano.si.edu/world/>). Last accessed on August 2012.
- 613 Strozzi, T., A. Luckman, T. Murray, U. Wegmüller, & C. L. Werner. (2002).
614 Glacier motion estimation using satellite-radar offset-tracking procedures,
615 *IEEE. Trans. Geosci. Remote Sens.*, 40(11), 2834–2391.
- 616 Strozzi, T., A. Kouraev, A. Wiesmann, U. Wegmüller, A. Sharov, & C. L.
617 Werner. (2008). Estimation of Arctic glacier motion with satellite L-band
618 SAR data, *Remote Sens. Environ.*, 112, 636–645.

619 Sundal, A. V., A. Shepherd, P. Niemow, E. Hanna, S. Palmer, & P.
620 Huybrechts. (2011). Melt-induced speed-up of Greenland ice sheet offset
621 by efficient subglacial drainage, *Nature*, 469, 521–524, [http://dx.doi.org/](http://dx.doi.org/10.1038/nature09740)
622 10.1038/nature09740.

623 Thompson, L. G., E. Mosley-Thompson, M. E. Davis, P. N. Lin, J. Dai, &
624 J. F. Bolzan. (1995). A 1000 year climatic ice-core record from the Guliya
625 ice cap, China: its relationship to global climate variability, *Ann. Glaciol.*,
626 21, 175–181.

627 Tobita, M., H. Suito, T. Imakiire, M. Kato, S. Fujiwara, & M. Murakami.
628 (2006). Outline of vertical displacement of the 2004 and 2005 Sumatra earth-
629 quakes revealed by satellite radar imagery, *Earth Planets Space*, 58, e1–e4.

630 Truffer, M., W. D. Harrison, & K. A. Echelmeyer. (2000). Glacier motion
631 dominated by processes deep in underlying till, *J. Glaciol.*, 46, 213–221.

632 WGMS and NSIDC. (1989). updated 2012. World Glacier Inventory. Com-
633 piled and made available by the World Glacier Monitoring Service, Zurich,
634 Switzerland, and the National Snow and Ice Data Center, Boulder CO,
635 U.S.A. [http://dx.doi.org/ 10.7265/N5/NSIDC-WGI-2012-02](http://dx.doi.org/10.7265/N5/NSIDC-WGI-2012-02).

636 Zhang, Z., & K. Jiao. (1987). Modern glaciers on the south slope of West
637 Kunlun Mountains (in Aksayqin Lake and Guozha Co Lake drainage areas),
638 *Bull. Glacier Res.*, 5, 85–91.

639 Zheng, B., H. Fushimi, K. Jiao, & S. Li. (1989). Characteristics of basal
640 till and the discovery of tephra layers in the West Kunlun Mountains, *Bull.*
641 *Glacier Res.*, 7, 177–186.

642 Zheng, B., J. Chen, & Y. Ageta. (1988). The preliminary report of Sino-
643 Japanese Joint Glaciological Expedition in the West Kunlun Mountains
644 1987, *Bull. Glacier Res.*, 6, 75–80.

645 Zwally, H. J., W. Abdalati, T. Herring, K. Larson, J. Saba, & K. Stef-
646 fen. (2002). Surface melt-induced acceleration of Greenland ice-sheet flow,
647 *Science*, 297, 218–222, [http://dx.doi.org/ 10.1126/science.1072708](http://dx.doi.org/10.1126/science.1072708).

Table 1: Details of the processed image pairs

Sensor/Path	Pair #	Master	Slave	Mode	Bperp (m) ^a	Span (d) ^b	Mean SNR ^c	% of pixel ^d
PALSAR/515 ^e	1	09/10/2007	12/11/2007	FBD-FBS	-619.6	92	7.5	76.1
	2	12/11/2007	01/26/2008	FBS-FBS	-284.2	46	14.6	90.5
	3	01/26/2008	04/27/2008	FBS-FBD	-1196.8	92	9.1	83.6
	4	04/27/2008	06/12/2008	FBD-FBD	7080.5	46	6.2	40.6
	5	06/12/2008	07/28/2008	FBD-FBD	-3734.3	46	6.6	45.4
	6	07/28/2008	12/13/2008	FBD-FBS	1141.2	138	7.3	74.3
	7	12/13/2008	01/28/2009	FBS-FBS	-261.8	46	14.8	91.6
	8	01/28/2009	06/15/2009	FBS-FBD	-659.9	138	7.0	73.9
	9	06/15/2009	12/16/2009	FBD-FBS	-1013.3	184	7.1	77.8
	10	12/16/2009	01/31/2010	FBS-FBS	-531.8	46	15.7	92.0
	11	01/31/2010	02/03/2011	FBS-FBS	-1772.6	368	10.5	91.1
PALSAR/516 ^e	12	02/09/2007	08/12/2007	FBS-FBD	-747.7	184	6.8	80.0
	13	08/12/2007	09/27/2007	FBD-FBD	-162.5	46	8.3	72.1
	14	09/27/2007	12/28/2007	FBD-FBS	-340.9	92	8.5	89.0
	15	12/28/2007	05/14/2008	FBS-FBD	-1464.3	138	7.9	87.8
	16	05/14/2008	06/29/2008	FBD-FBD	2819.0	46	6.6	48.2
	17	06/29/2008	09/29/2008	FBD-FBD	1646.4	92	6.9	67.2
	18	09/29/2008	11/14/2008	FBD-FBS	-380.7	46	9.2	83.3
	19	11/14/2008	12/30/2008	FBS-FBS	1.3	46	15.2	97.3
	20	12/30/2008	02/14/2009	FBS-FBS	710.3	46	14.6	96.7
	21	02/14/2009	08/17/2009	FBS-FBD	-397.8	184	7.7	79.0
	22	08/17/2009	10/02/2009	FBD-FBD	-502.3	46	10.0	74.1
	23	10/02/2009	01/02/2010	FBD-FBS	-585.9	92	9.2	92.5
	24	01/02/2010	02/20/2011	FBS-FBS	-2605.9	414	9.2	87.9
ASAR/248 ^f	25	11/07/2003	12/12/2003	IS2	283.7	35	9.0	49.4
	26	09/17/2004	10/22/2004	IS2	38.9	35	9.5	70.3
	27	03/11/2005	04/15/2005	IS2	-62.7	35	8.9	64.8
	28	01/20/2006	03/31/2006	IS2	17.9	70	8.7	74.2
	29	03/16/2007	04/20/2007	IS2	-386.4	35	7.2	53.5

Table 2: Classification of the 36 examined glaciers in West Kunlun Shan

Slope	Glacier Name	Glacier ID	Glacier data (NSICD WGI ^a)						Flow line data				Winter mean/max velocity (m/yr)
			max elev. (m)	min elev. (m)	max length (km)	mean grad. (deg)	max elev. (m)	min elev. (m)	max length (km)	mean grad. (deg)			
Normal flow													
north	N1	CN5Y641H0088	6309	5350	6.5	8.4	5920	5391	5.2	5.9	8/11±2		
north	West Kunlun (western branch)	CN5Y641H0074	6522	5120	18.5	4.3	6025	5312	12.2	3.4	13/21±3		
north	Kunlun (western branch)	CN5Y641G0055	6785	4882	23.6	4.6	6210	4845	23.0	3.5	10/23±2		
north	Kunlun (eastern branch)	CN5Y641G0055	6785	4882	23.6	4.6	6260	4845	22.2	3.7	32/51±4		
north	N3	CN5Y641G0038	6792	5054	19.0	5.2	6310	5172	17.3	3.7	44/67±7		
north	Duofeng	CN5Y641G0023	6957	4590	31.0	4.4	6355	4732	28.0	3.3	41/73±5		
north	N4 ^b	-	-	-	-	-	6349	5310	13.7	4.5	27/42±6		
north	N5	CN5Y641F0098	6734	4810	20.0	5.5	6323	4946	17.1	4.5	33/49±7		
north	N6	CN5Y641F0085	6093	4940	26.1	2.5	6447	4935	24.1	3.6	21/40±3		
north	Yulong	CN5Y641F0063	6778	5140	30.9	3.0	6459	5072	29.6	2.6	9/16±2		
north	Xiezhic	CN5Y641F0049	6362	5480	13.1	3.9	6171	5479	12.2	3.2	8/13±1		

(continued)

(continued)

north	Alakesayi ^c	CN5Y641F0046	6786	5280	18.5	4.7	6129	5374	14.0	3.3	23/36±3
north	Yake ^c	CN5Y641F0023	6597	5230	14.5	5.4	6271	5336	13.3	4.1	19/36±3
south	S1	CN5Z433B0033	6343	5440	8.3	6.2	6033	5473	6.6	4.8	8/13±3
south	Quanshui	CN5Z433B0047	6386	5470	10.8	4.8	6060	5469	8.6	3.9	12/19±2
south	Bingshuihe	CN5Z433C0005	6546	5450	16.2	3.9	6062	5603	4.7	5.1	13/24±3
south	Litian	CN5Z433D0004	6433	5400	10.0	5.9	6155	5381	9.0	4.9	19/29±5
south	Guozha	CN5Z431B0014	6530	5390	13.1	5.0	6242	5373	12.4	3.9	31/57±8
south	S2	CN5Z431C0008	6810	5460	16.2	4.8	6301	5462	13.2	3.7	12/17±2
south	S3	CN5Z431C0012	6489	5590	6.8	7.5	6109	5605	6.1	4.7	7/11±2
south	S4 ^b	CN5Z431C0016 ^d	-	-	-	-	6198	5452	8.3	5.1	14/27±4
south	S5 ^b	-	-	-	-	-	6138	5542	11.1	3.1	12/20±2
south	S6 ^b	-	-	-	-	-	6184	5563	5.3	6.7	18/39±8
south	S7 ^b	-	-	-	-	-	6350	5536	9.2	5.1	22/40±6
south	S8	CN5Y636J0086	6667	5520	8.3	7.9	6346	5526	7.6	6.6	22/46±8

Surging

north	West Kunlun	CN5Y641H0074	6522	5120	18.5	4.3	6060	5237	14.0	3.4	92/161±14
north	N2	CN5Y641H0067	6440	5277	15.1	4.4	6223	5319	13.2	3.8	78/195±20
north	N7 ^b	CN5Y641F0073 ^d	-	-	-	-	6398	4747	15.9	6.1	72/207±38

(continued)

(continued)

south	Zhongfeng (branch1)	CN5Z433D0008	7167	5400	23.4	4.3	6262	5353	17.0	3.0	15/35±3
Stagnant flow											
north	West Yulong	CN5Y641G0068	6532	5140	21.9	3.6	6155	5151	20.4	2.8	10/19±2
south	Douta	CN5Z433C0020	6498	5440	15.6	3.9	6170	5486	13.3	2.9	8/13±2
south	Gongxing	CN5Z433C0027	6721	5360	20.5	3.8	6261	5339	17.3	3.0	9/18±2
south	Zhongfeng (branch2)	CN5Z433D0008	7167	5400	23.4	4.3	6294	5353	17.0	3.1	8/21±2
south	Zhongfeng (branch3)	CN5Z433D0008	7167	5400	23.4	4.3	6453	5353	16.3	3.8	11/34±2
south	Zhongfeng (branch4)	CN5Z433D0008	7167	5400	23.4	4.3	6250	5353	20.5	2.5	16/42±3
south	Chongce	CN5Z431C0001	6903	5320	28.7	3.2	6421	5330	25.7	2.5	13/39±2

Table 1: a: Orbit separation distance perpendicular to the radar line-of-sight. b: Temporal separation. c: Lower SNR less than 5.0 was rejected. d: Percentage of accepted pixels. e: Ascending track of ALOS/PALSAR. f: Descending track of Envisat/ASAR.

Table 2: Classification of the 36 examined glaciers in West Kunlun Shan. a: NSIDC world glacier inventory (http://nsidc.org/data/glacier_inventory), b: No data are available from WGI, c: Ma et al [1989], d: Zheng et al [1989]

Figure 1: Study area and ALOS/PALSAR (path 515 and 516) and Envisat ASAR (path 248) data coverage in this study; see Table 1. Inset shows the location of the Tibetan plateau and the analyzed area.

Figure 2: Principle of the RGB (Red, Green, and Blue) method. (a) Old radar scattering intensity image. (b) New intensity image. (c) Old intensity image marked with cyan. (d) Newer intensity image marked with red. (e) Composite image after the RGB addition of the intensity images (c) and (d). While the red/cyan areas show where the surface scattering intensities have increased/decreased, areas that underwent no intensity changes remain gray.

Figure 3: A sample glacier surface velocity map at West Kunlun Shan overlaid on the PALSAR-based scattering intensity image. Note that the scale is logarithmic. The velocity estimates are derived from November 12, 2008 to December 30, 2008 for the western area (path 516) and from December 12, 2008 to January 28, 2009 for the eastern area (path 515); see Table 1. The examined glacier names and the Guliya icecap are indicated. Thin black lines denote flow lines, and magenta lines are the divides in the middle.

Figure 4: Surface velocity evolution at the Duofeng Glacier. (a) Spatial–temporal evolution of the surface velocities recorded from 2003 to 2011. (b) Error estimates of (a). (c) Average velocity profiles for summer (red) and winter (blue). The 'x' symbols are the values used in the computation of the summer and winter average. (d) The elevation and local gradient profiles along the chosen flow line.

Figure 5: Surface velocity evolution at the N3 Glacier. (a) Spatial–temporal evolution of the surface velocities recorded from 2003 to 2011. (b) Error estimates of (a). (c) Average velocity profiles for summer (red) and winter (blue). The 'x' symbols are the values used in the computation of the summer and winter average. (d) The elevation and local gradient profiles along the chosen flow line.

Figure 6: Surface velocity evolution at the western branch of the Kunlun Glacier. (a) Spatial-temporal evolution of the surface velocities recorded from 2003 to 2011. (b) Error estimates of (a). (c) Average velocity profiles for summer (red) and winter (blue). The 'x' symbols are the values used in the computation of the summer and winter average. (d) The elevation and local gradient profiles along the chosen flow line.

Figure 7: Surface velocity evolution at the Yulong Glacier. (a) Spatial–temporal evolution of the surface velocities recorded from 2003 to 2011. (b) Error estimates of (a). (c) Average velocity profiles for summer (red) and winter (blue). The 'x' symbols are the values used in the computation of the summer and winter average. (d) The elevation and local gradient profiles along the chosen flow line.

Figure 8: Surface velocity evolution at the eastern branch of the Kunlun Glacier. (a) Spatial–temporal evolution of the surface velocities recorded from 2003 to 2011. (b) Error estimates of (a). (c) Average velocity profiles for summer (red) and winter (blue). The 'x' symbols are the values used in the computation of the summer and winter average. (d) The elevation and local gradient profiles along the chosen flow line.

Figure 9: Surface velocity evolution at the westernmost tributary of Zhongfeng Glacier. (a) Spatial–temporal evolution of the surface velocities recorded from 2003 to 2011. (b) Error estimates of (a). (c) Average velocity profiles for summer (red) and winter (blue). The 'x' symbols are the values used in the computation of the summer and winter average. (d) The elevation and local gradient profiles along the chosen flow line.

Figure 10: RGB composite intensity image of an old image obtained on February 9, 2007 and a new image obtained on February 20, 2011. Cyan-colored area indicates a reduction in the scattering intensity.

Figure 11: Surface velocity evolution at the West Kunlun Glacier. (a) Spatial–temporal evolution of the surface velocities recorded from 2003 to 2011. (b) Error estimates of (a). (c) Average velocity profiles for summer (red) and winter (blue). The 'x' symbols are the values used in the computation of the summer and winter average. (d) The elevation and local gradient profiles along the chosen flow line.

Figure 12: Surface velocity evolution at the N2 Glacier. (a) Spatial–temporal evolution of the surface velocities recorded from 2003 to 2011. (b) Error estimates of (a). (c) Average velocity profiles for summer (red) and winter (blue). The 'x' symbols are the values used in the computation of the summer and winter average. (d) The elevation and local gradient profiles along the chosen flow line.

Figure 13: Terminus advances at the West Kunlun and N2 Glaciers recorded from ALOS/PALSAR intensity images.

Figure 14: RGB composite intensity image of an old image obtained on February 9, 2007 and a new image obtained on February 20, 2011. Red-colored area indicates an increase in the scattering intensity.

Figure 15: Surface velocity evolution at the Chongce Glacier. (a) Spatial-temporal evolution of the surface velocities recorded from 2003 to 2011. (b) Error estimates of (a). (c) Average velocity profiles for summer (red) and winter (blue). The 'x' symbols are the values used in the computation of the summer and winter average. (d) The elevation and local gradient profiles along the chosen flow line.

Figure 16: Surface velocity evolution at the West Yulong Glacier. (a) Spatial-temporal evolution of the surface velocities recorded from 2003 to 2011. (b) Error estimates of (a). (c) Average velocity profiles for summer (red) and winter (blue). The 'x' symbols are the values used in the computation of the summer and winter average. (d) The elevation and local gradient profiles along the chosen flow line.

Figure 17: Surface velocity evolution at the second branch of the Zhongfeng Glacier. (a) Spatial-temporal evolution of the surface velocities recorded from 2003 to 2011. (b) Error estimates of (a). (c) Average velocity profiles for summer (red) and winter (blue). The 'x' symbols are the values used in the computation of the summer and winter average. (d) The elevation and local gradient profiles along the chosen flow line.

Figure 1

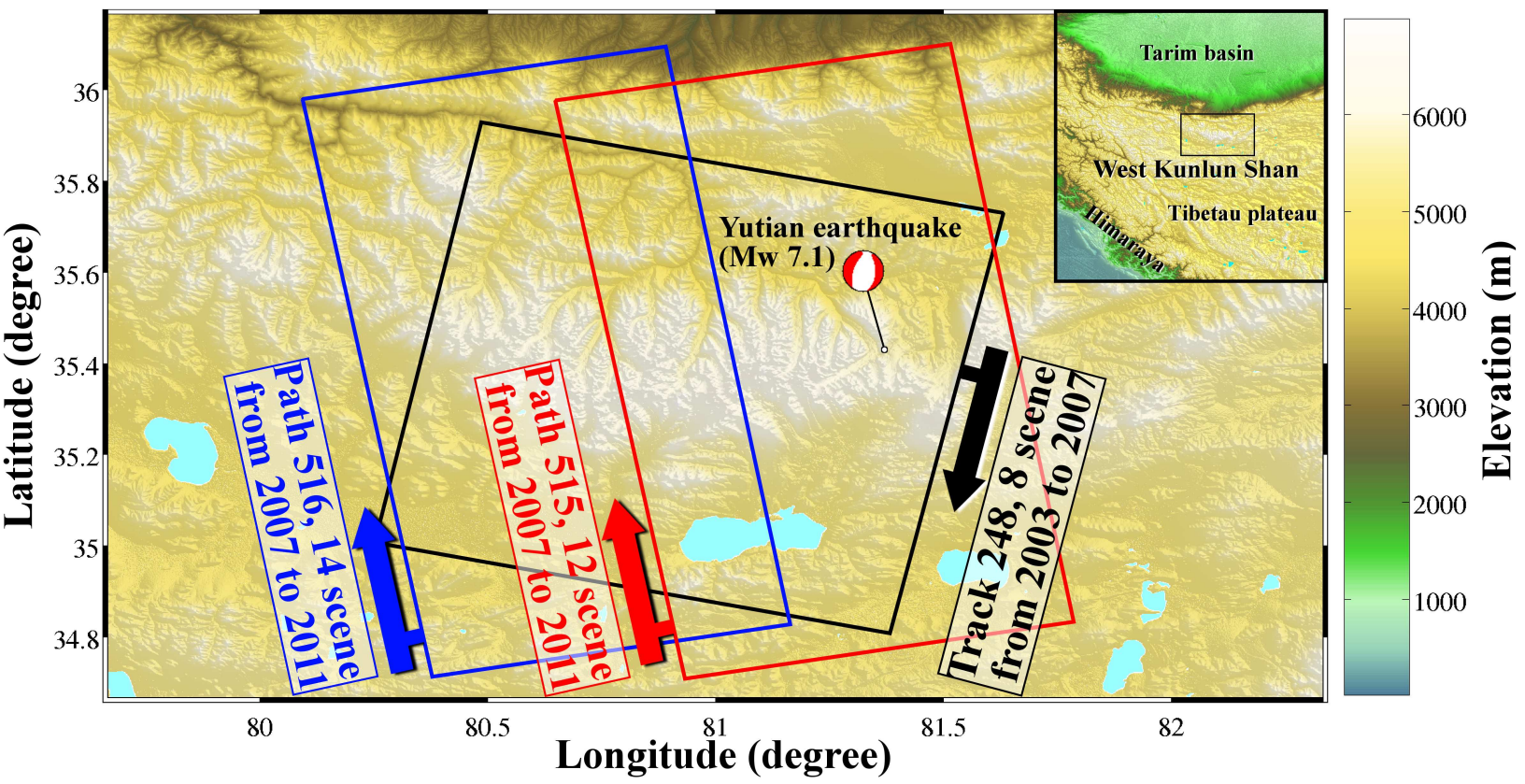
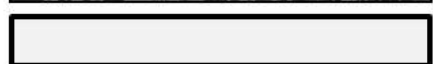
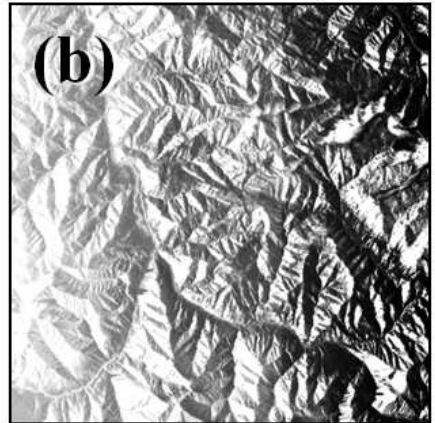


Figure 2

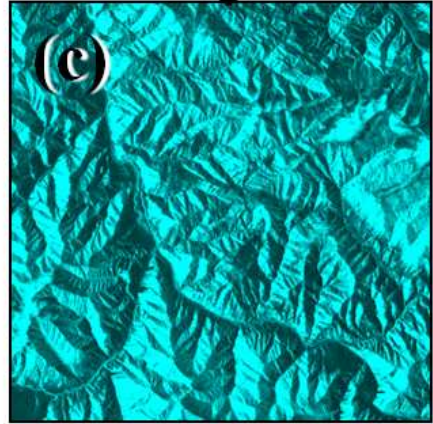
Master SAR intensity image

Slave SAR intensity image



intensity

+ intensity -



intensity

+ intensity -

(R,G,B)=(0, Master, Master)

(R,G,B)=(Slave, 0, 0)

RGB composed image

+

=



+ intensity -

(R,G,B)=(Slave, Master, Master)

Figure 3

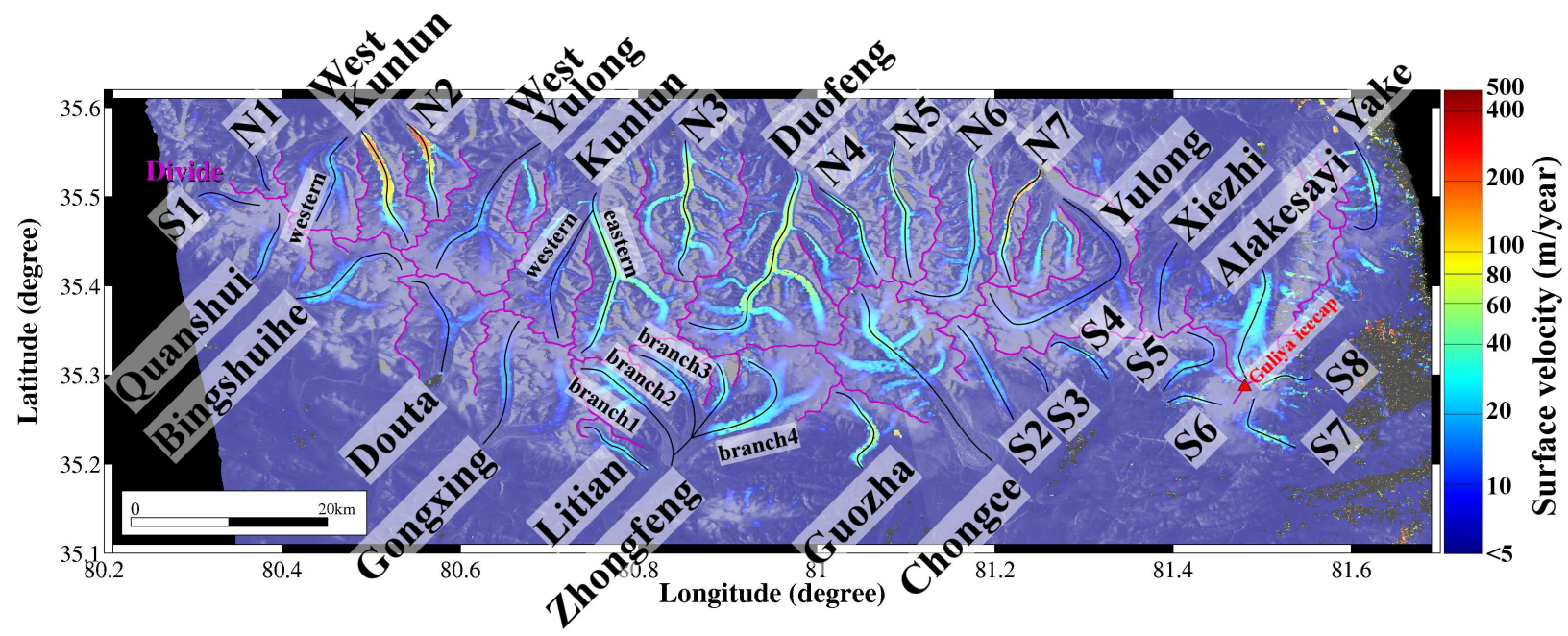


Figure 4

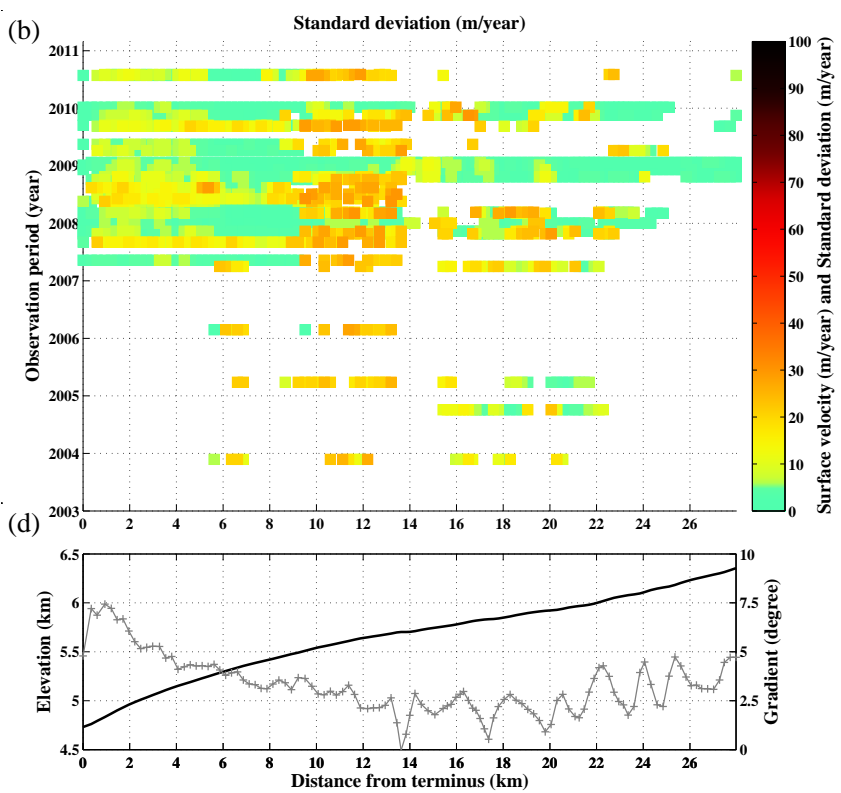
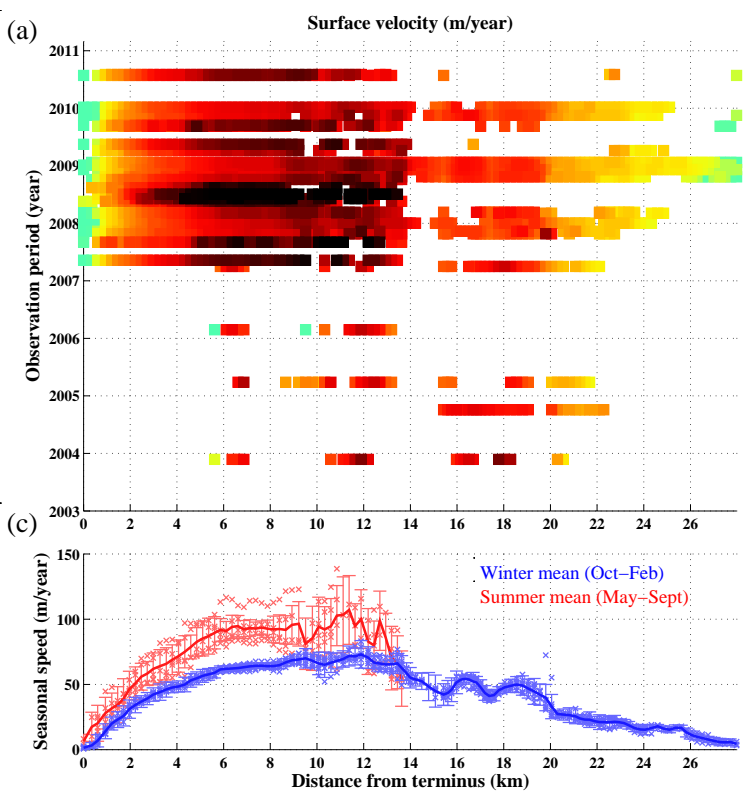


Figure 5

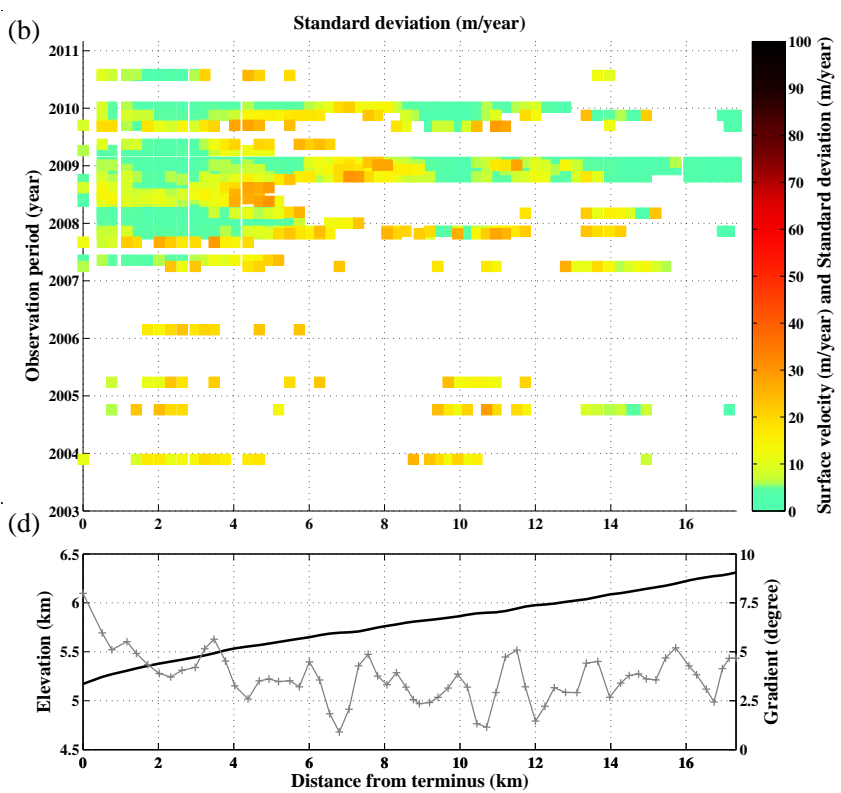
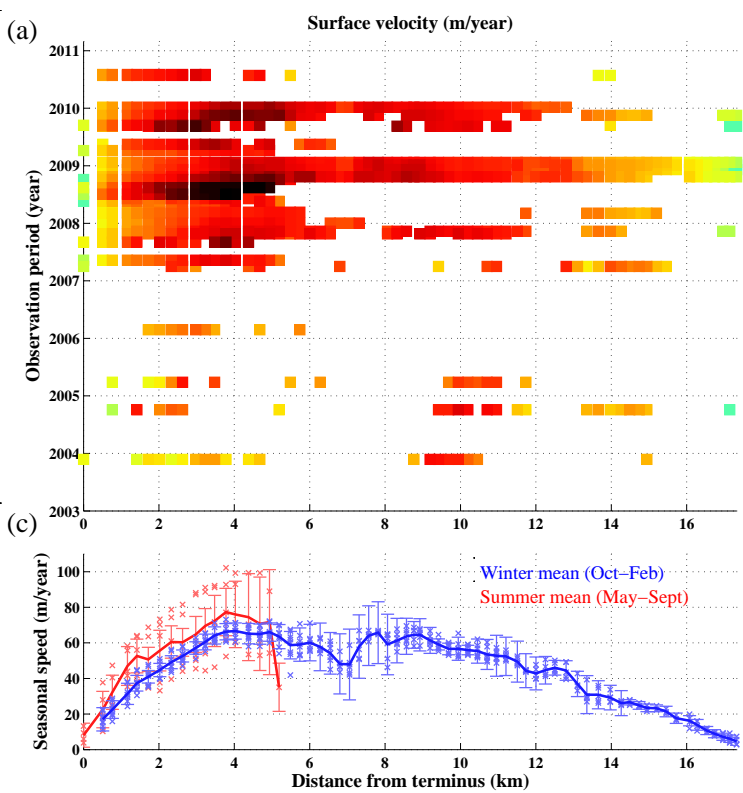


Figure 6

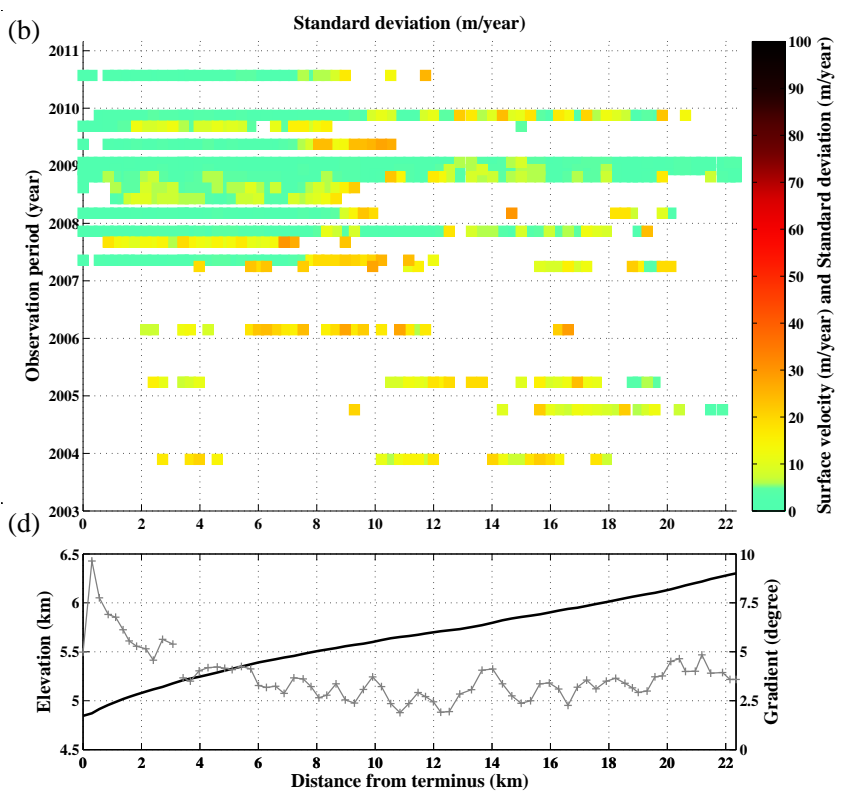
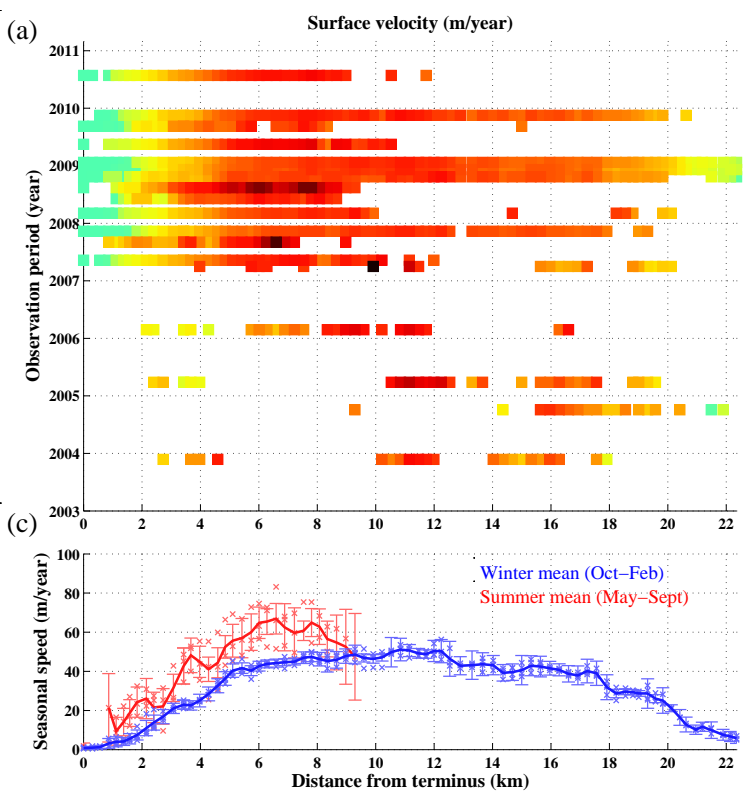


Figure 7

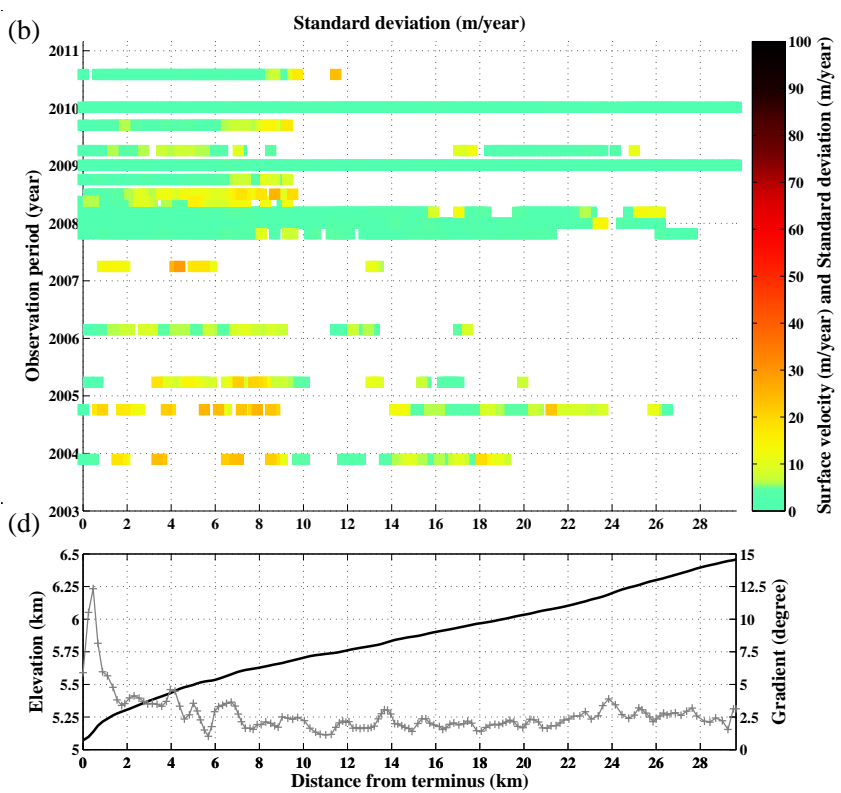
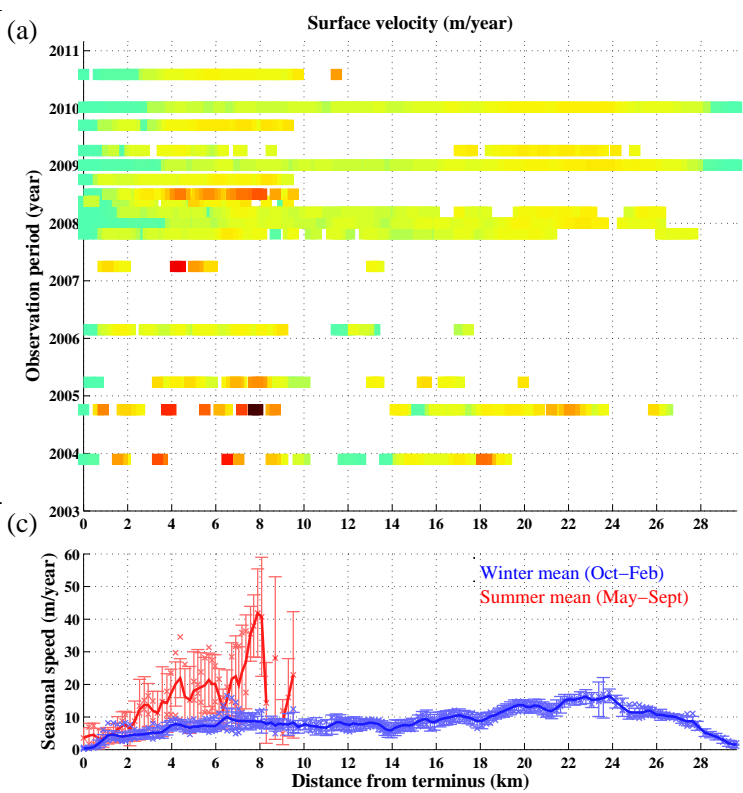


Figure 8

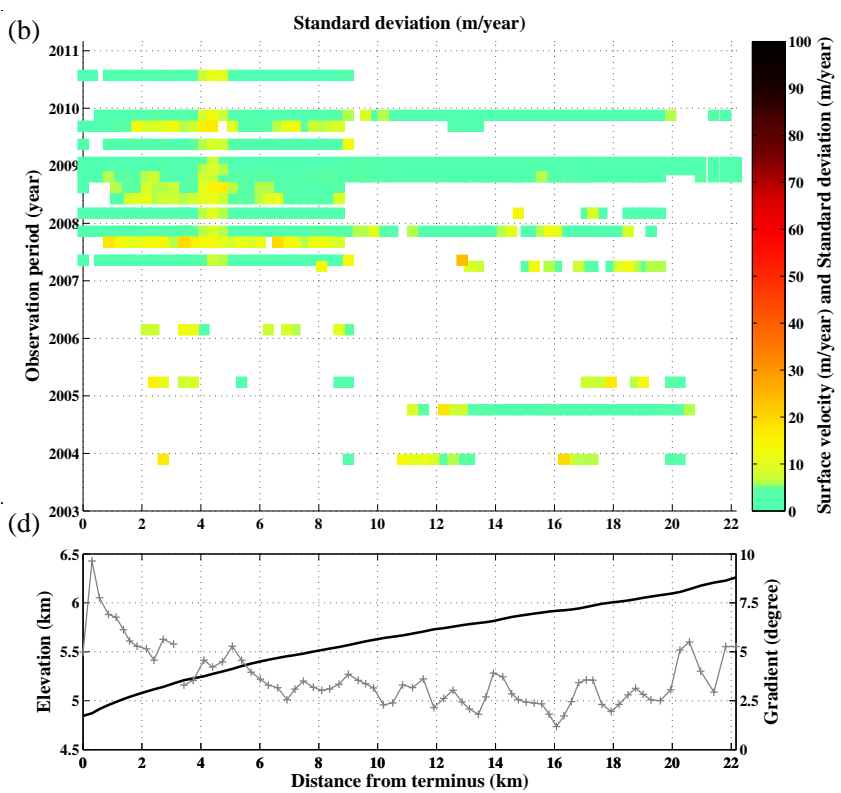
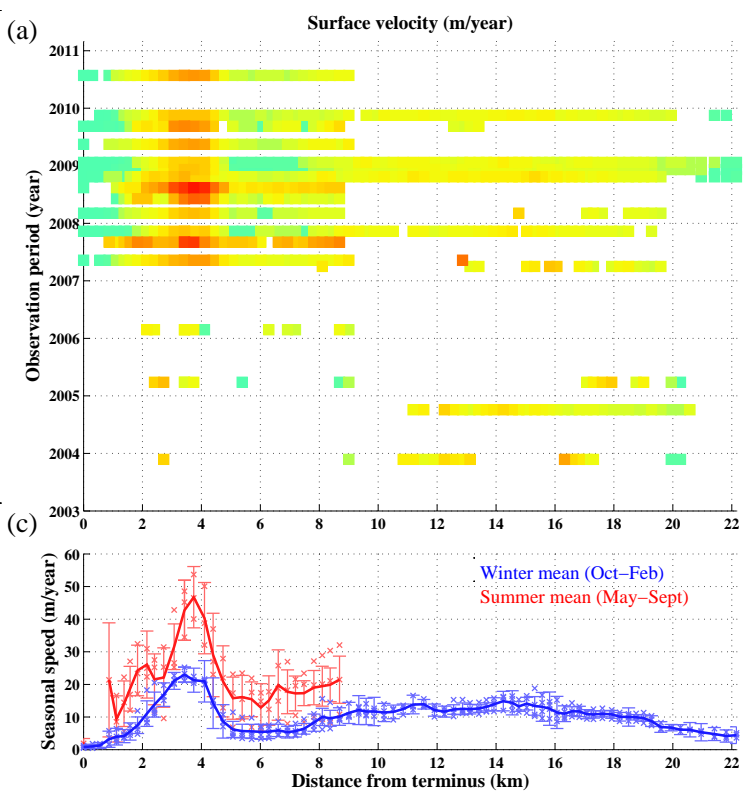


Figure 9

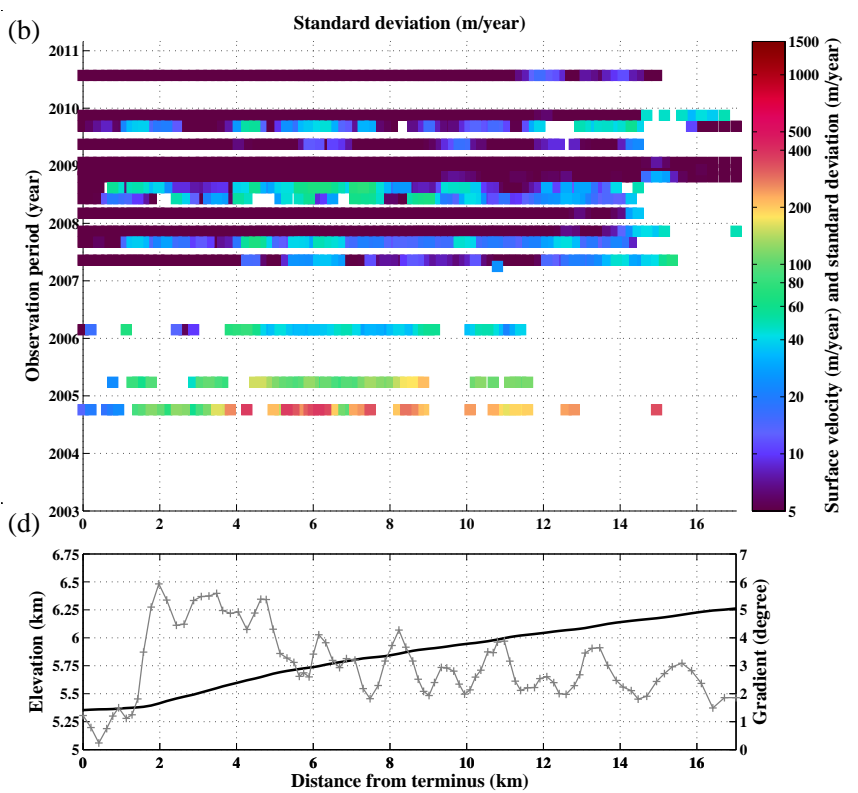
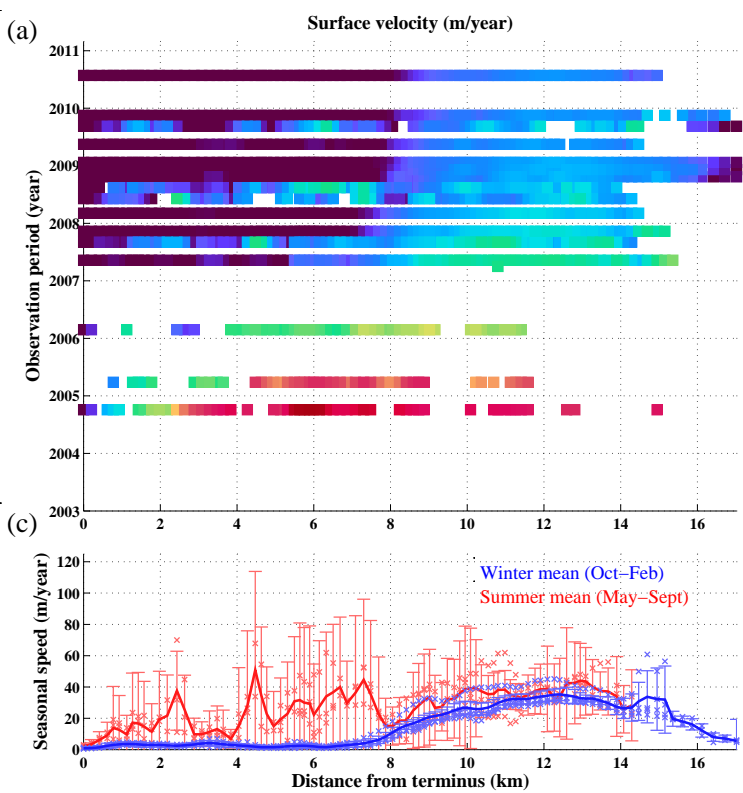


Figure 10

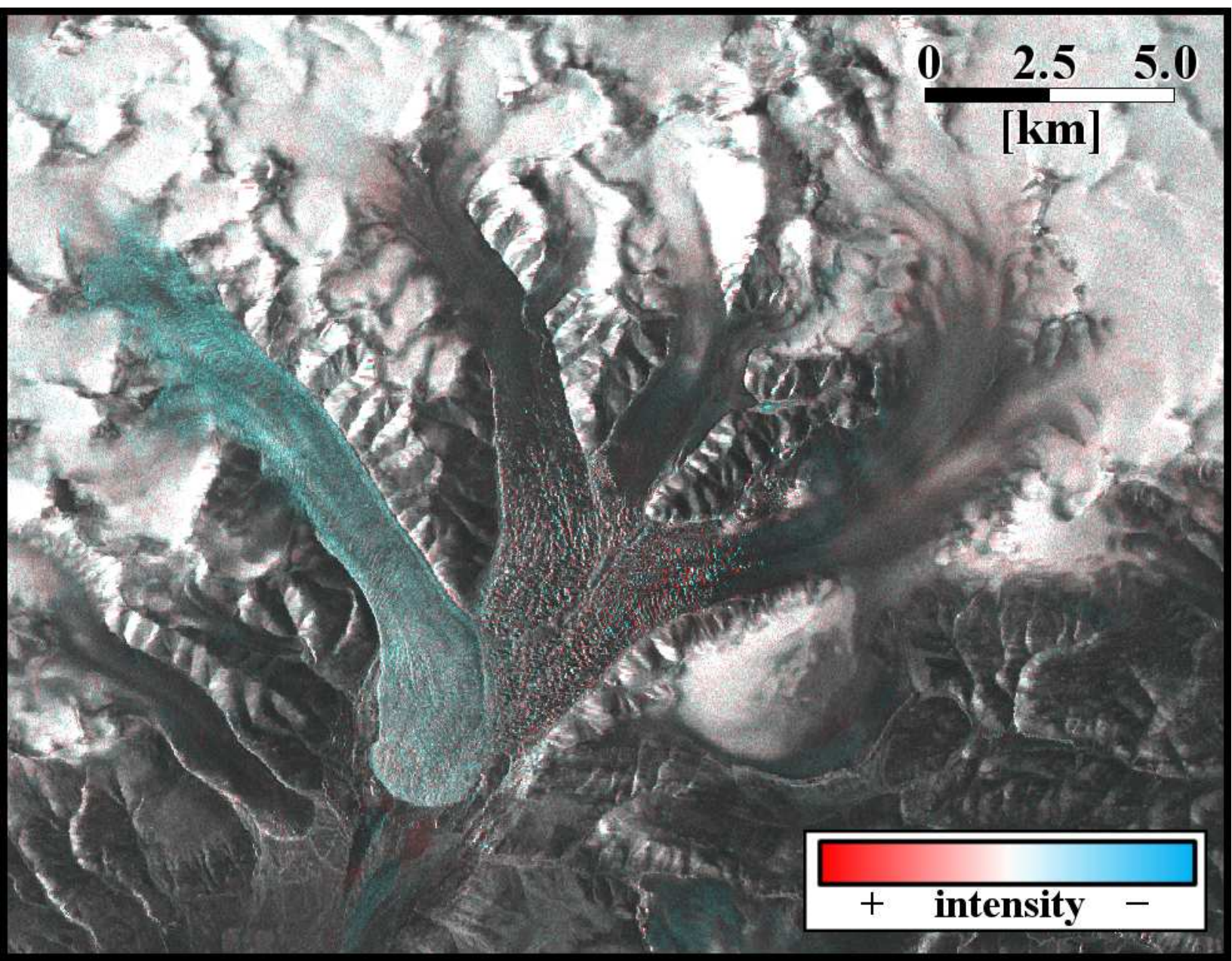


Figure 11

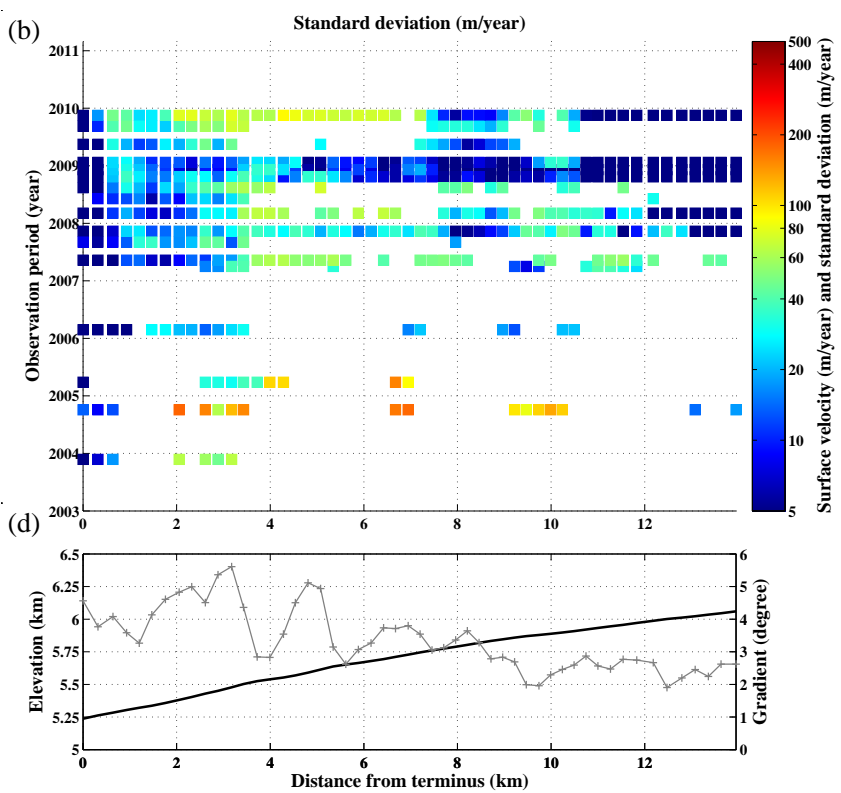
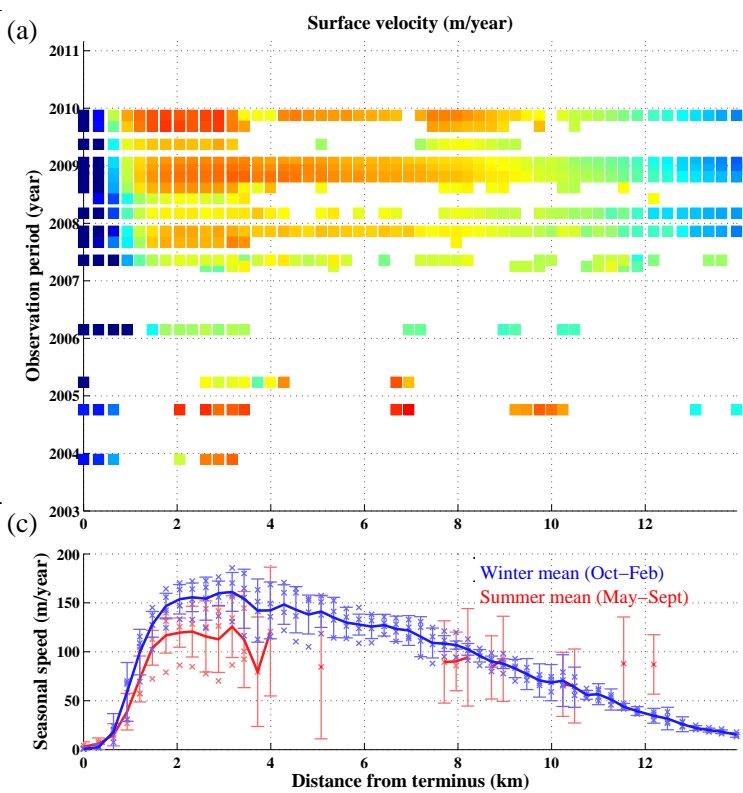


Figure 12

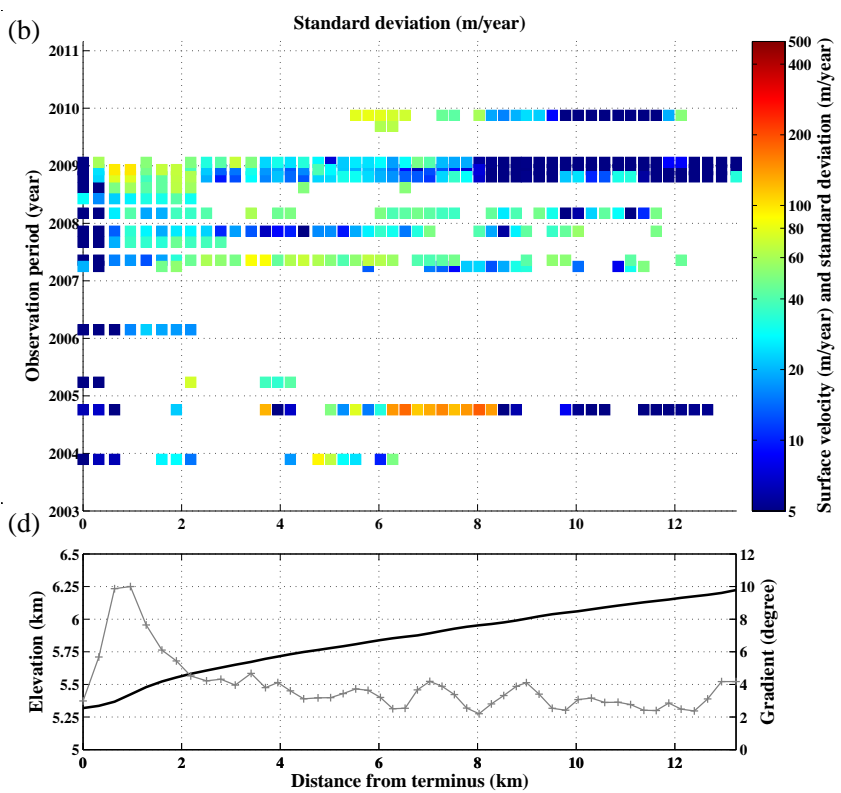
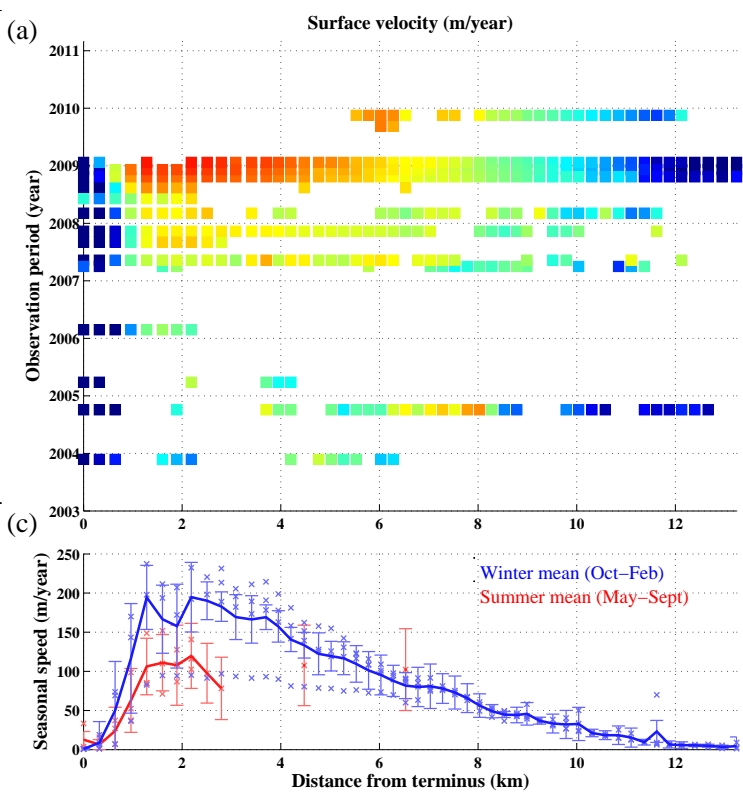


Figure 13

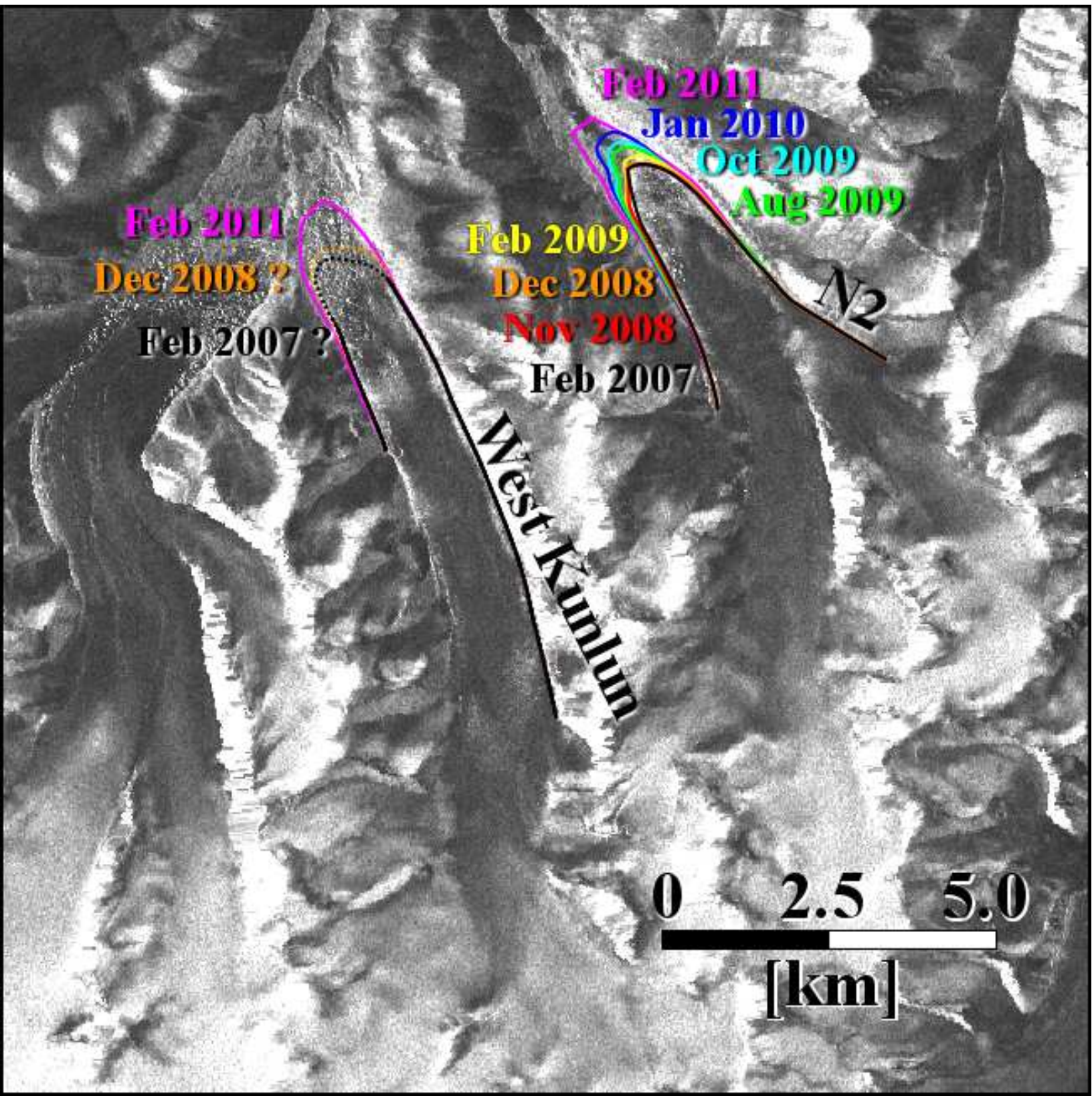


Figure 14

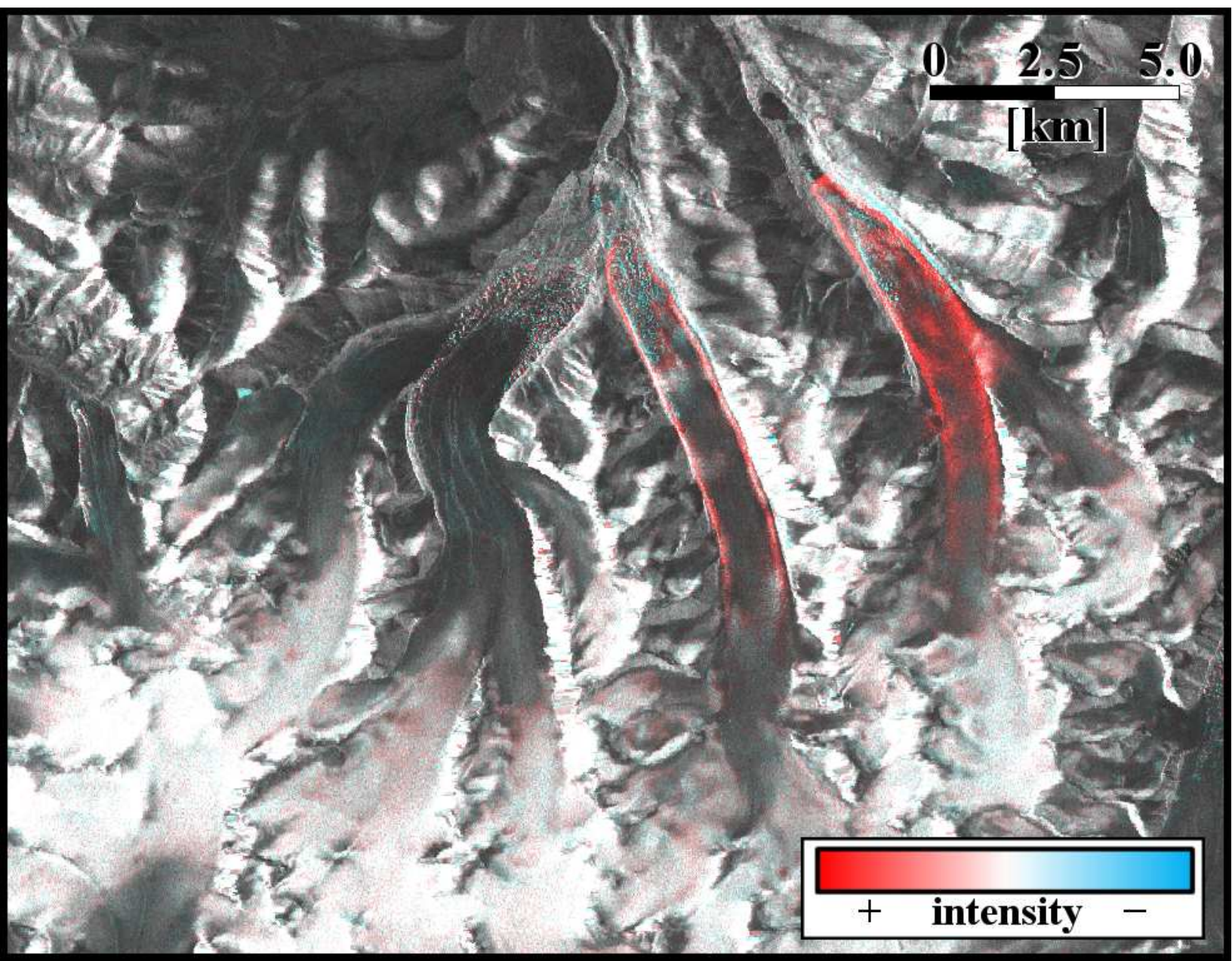


Figure 15

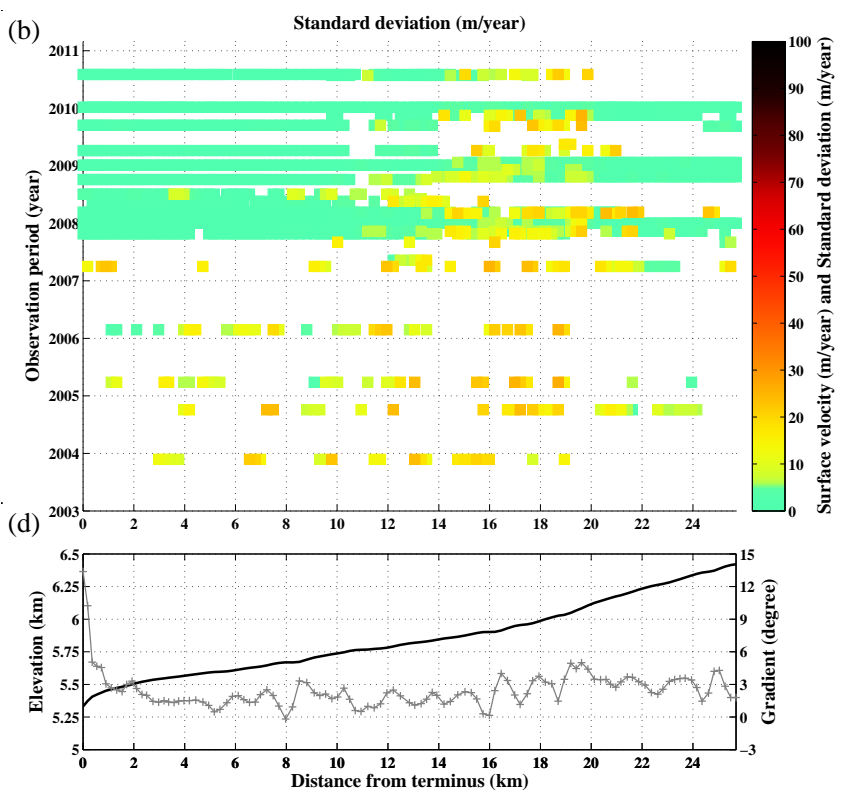
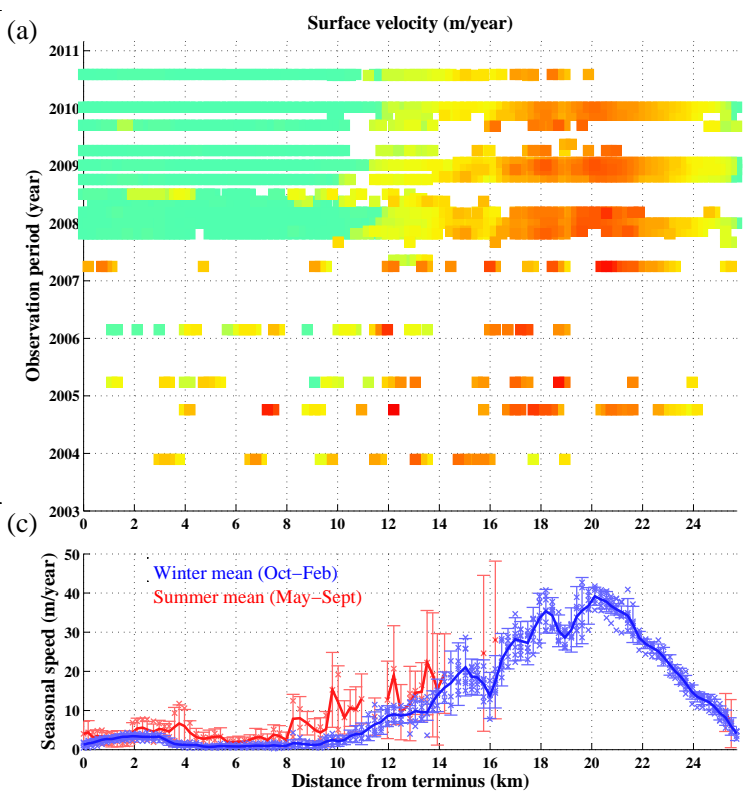


Figure 16

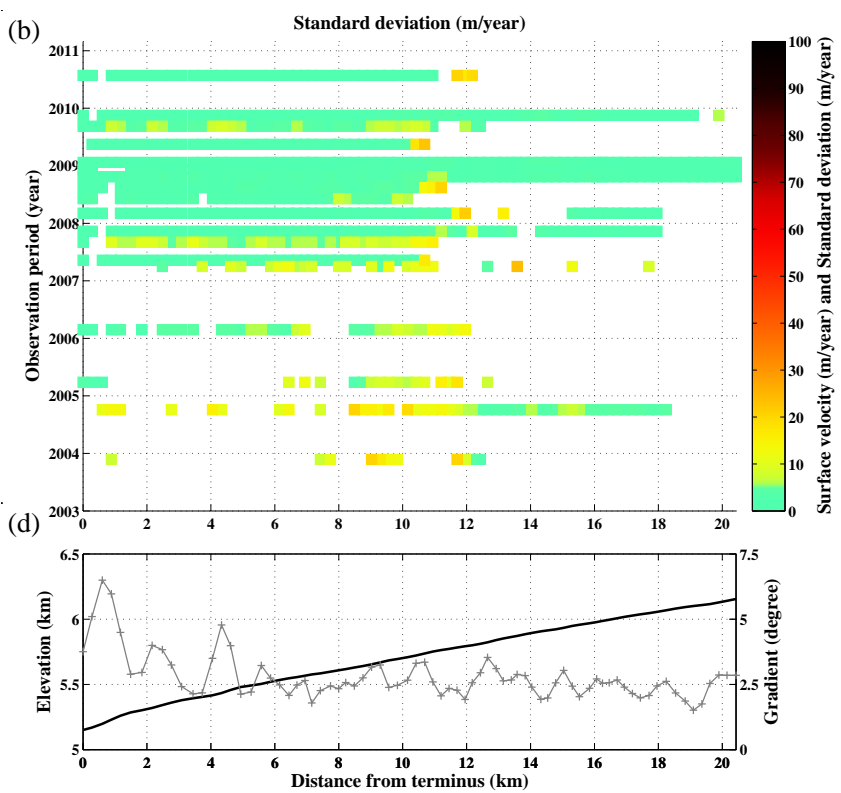
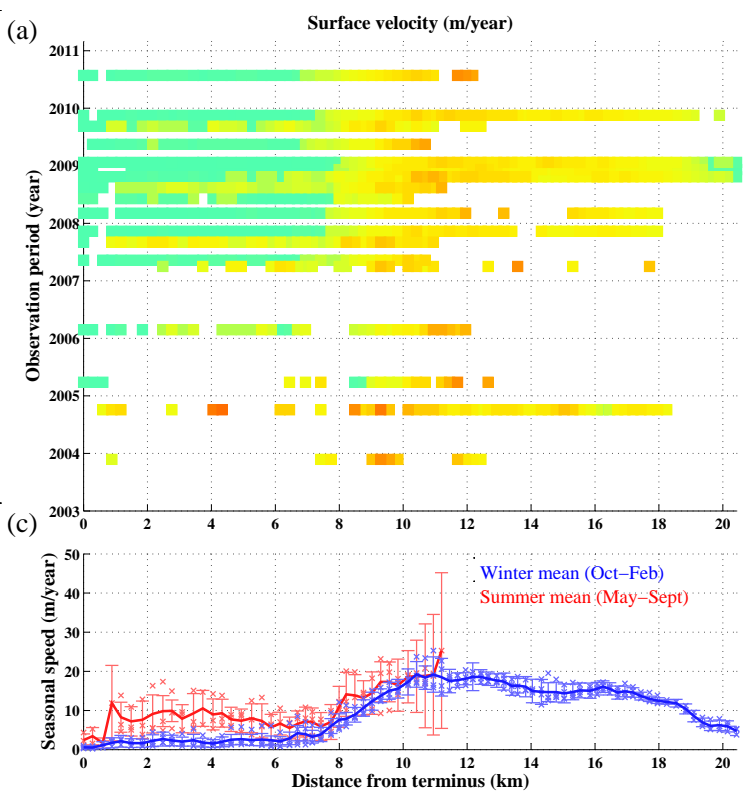


Figure 17

